Mapping material-property space of cellular metamaterials under uncertainty

Sheng Liu*, Pinar Acar

Department of Mechanical Engineering, Virginia Polytechnic Institute and State University, 24061, Blacksburg, USA.

Abstract

Cellular mechanical metamaterials (CMMs) are assemblies of periodic representative volume elements which can be engineered to exhibit unique mechanical properties. Recent advances in additive manufacturing (AM) have enabled us to fabricate sophisticated architected materials with high precision. To increase and diversify applications in both science and engineering practice, the rapid development of fabrication technologies necessities a novel and effective algorithm to outline a theoretical property space for material design problems, allowing designers to acknowledge the limitations of material performance, and to make informed trade-off between target objectives and competing industrial requirements. Inspired by biological evolution, the proposed work addresses a methodology for intuitively mapping material-property spaces of CMMs by using the genetic algorithm as a sampling algorithm, consisting selection of objective properties and stochastic search of property points. It approximates the property space more faithfully and comprehensively than traditional mapping approaches. Considering the manufacturing defects of the AM, uncertainties in properties are quantified via the deep learning method. Variations of properties induced by the defects are illustrated as stochastic boundaries of the property space.

Keywords: Cellular metamaterials; Material property space; Uncertainty effects; Genetic algorithm; Neural network; Numerical homogenization

1. Introduction

Cellular materials widely exist in natural biological systems such as honeycombs, bones, and woods [1]. Owing to their unique features, including high stiffness and low density [2], they are commonly applied in aerospace [3, 4] and transportation [5, 6] industries as structural panels. Over the past decade, advances in additive manufacturing have enabled engineers to precisely control the characteristic material behavior on the macro-scale by tailoring the geometric arrangements on the micro-scale. Tailoring the geometrical arrangements of the metamaterials dramatically increases the design domain in engineering applications and produces a wide variety of metamaterials. For example, auxetic metamaterials with chiral and anti-chiral configurations exhibit a negative Poisson ratio [7]. Porous metamaterials containing periodically circular pores demonstrate high-energy absorb behavior [8]. Lattice metamaterials constructed by nodes and struts show excellent scaling of stiffness and strength with respect to their weight [9]. Among these various kinds of metamaterials, engineers require an intuitive tool/reference to select appropriate types of metamaterials to satisfy particular application demands in science or engineering practice.

Material property space serves as a valuable tool/reference for material selection. Similar to Ashby's chart [10], it is a complete envelope that summarizes theoretically possible combinations of properties, denoted as experimental points in the space. Its area represents the availability of the combined performance of a particular family of metamaterials. Referring to their corresponding areas, engineers can check the limitation of the combined performances of materials and compare them from one family to another to intuitively select an appropriate material. Furthermore, the overlapping area between two property spaces provides alternative solutions for the materials for similar engineering

*Corresponding author

Email address: sheng120@vt.edu (Sheng Liu)

purposes. It increases the freedom of the fabrication process and allows engineers to make trade-offs between target objectives and competing industrial requirements. In addition to material selections, exploring a comprehensive material-property space is essential to machine learning (ML). For an inverse problem, an ML model cannot extrapolate well outside the training data domain [11]. In other words, if the input properties are not within the training data domain, an ML model cannot achieve high accuracy for the prediction of the corresponding geometrical arrangement of the material even if the model is well-trained. Therefore, the applicability of an ML model depends not only on the architecture of the model itself but also on the region of its training data domain [11]. For a particular material system, its comprehensive property space could provide a guideline to construct a database and improve the applicability of its trained model in an inverse problem.

Analytical methods generate the property space by using bounding theories such as the Hashin-Shtrikman bounds [12], and the Voigt [13] and Reuss [14] bounds. These theories predict points that are exterior to the bounds to expand the property space. However, the points are non-physical and might not correspond to physically realizable microstructures. What's more, the bound determined by these theories is for a single property instead of simultaneous combinations of properties. Thus, it is infeasible to employ these theories to plot the property space in 2D and higher dimensions. Some computational methods utilize uniform sampling of geometric design variables to map the property space. It is a rapid method to generate numerous possible properties corresponding to their randomly generated microstructures. However, due to the central limit theorem, properties of sampled geometric patterns follow a Gaussian distribution, which causes the corresponding property points to be centrally located in a portion of the explored space. This reduces the efficiency of space exploration and produces a poor approximation of the property space. Pareto Front techniques can provide more accurate estimations of the property space. This technique applies various algorithms, including Adaptive Normal Boundary Intersection (ANBI), Adaptive Weighted Sum (AWS), and Generalized Weighted Sum (GWS) [15, 16, 17]. To explore the property space, these algorithms are facilitated with gradient-based optimization methods, such as simple quadratic programming for GWS and sequential quadratic programming for ANBI and AWS. The drawback of Pareto Front techniques is relying on appropriately selected initial guesses to process gradient-based optimization methods [18]. Their optimum solution might converge to the local solutions considering the complexity of the design space caused by complicated geometric arrangements of metamaterials. Moreover, the GWS can only identify points on convex surfaces, but the property space boundary might vary based on the distribution of property points from convex to concave surfaces.

To address the potential issues mentioned above, our study develops a systematical framework to explore materialproperty space using a genetic algorithm (GA). Traditionally, GA serves as a global optimization method to search extreme properties in forward problems [19, 20, 21] or to obtain optimal microstructures with target properties in inverse problems [22, 23, 24]. In these problems, after a stochastic search process of the GA, the engineers are usually interested in its final optimal solutions rather than its children generated in each generation. On the contrary, our framework employs the GA as a sampling algorithm to intuitively sample all possible microstructures (children of the GA) for a particular material system based on biological evolution. After computing the structural properties of these microstructures, the region of material-property space can be determined by bounding all of the resulting property points. Due to biological evolution [25], springs of the GA from new generations will eventually be evolved into property points that locate on or nearby the objective properties of the inverse problem. Inspired by that, our framework uses the objective properties to promote the GA to sample possible microstructures in locations of unexplored property spaces. It helps the sampling process generate possible property points exterior to the current incomplete property space. To this end, our framework relies on the sampling algorithm that iterates steps between the selection of objective properties (Fig. 1A) and the sampling of microstructures (Fig. 1B and 1C) to expand the property space progressively until the resulting property space is maximal. The property space is visualized in a 2D material-property chart (Fig. 1D). It contains all the possible combinations of two structural properties that are scattered in the same plot. Each axis of the chart represents the structural properties of a particular material system, such as Poisson's ratio and Young's modulus.

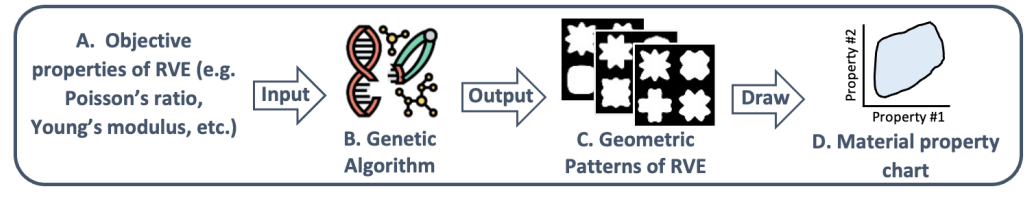
In this paper, to demonstrate its reliability and feasibility, the proposed framework is applied to explore material-property spaces of a special but widely used class of cellular mechanical metamaterials (CMMs), which is 2D porous cellular solids with periodic representative volume elements (RVEs) [26]. To perform material selections, this paper mainly focuses on two families of the CMMs, one with RVEs consisting of 4 periodic unit cells and another with RVEs consisting of 4 non-periodic unit cells shown in Fig 2. Compared to conventional non-architected structures, uncertainties in the physical responses of the CMMs are impacted more by variations in geometric patterns of their

RVEs owing to their complicated realization processes, such as Fused Deposition Modeling (FDM) and Fused Filament Fabrication (FFF) [27]. This work further studies the effects of manufacturing defects on the physical responses of CMMs, which lead to variations in the region of the property space. The uncertainty of the material-property space can be numerically quantified in various space areas determined by the Monte Carlo (MC) method. It can be visualized as a variation interval of the space boundary, which is the reign highlighted in yellow shown in Fig. 1I-a. During the cooling process of FFF/FDM, surface distortion appears for thermoplastic materials caused by various cooling rates and complex porous microstructures in RVEs [28]. Due to the unique features of the geometric parameters of the CMMs, slight variations in their values enable us to approximate the realization of this manufacturing defect. Considering expensive computations on structural properties, this study bypasses the finite element method and accelerates the MC sampling (Fig. 1F) by using a deep learning approach (Fig. 1G). The approach can effectively predict the structural properties (Fig. 1H) of various geometric patterns of the RVEs (Fig. 1E) realized by slight variations in the geometric parameters. The flowchart of the proposed framework is shown in Fig. 1.

The rest of the paper is organized as follows. In Section 2, we define the microstructures of our CMMs and their effective properties calculation by the homogenization method, develop a sampling method by genetic algorithm for space exploration, and propose the Monte Carlo (MC) method facilitated by a deep learning model for uncertainty quantification. In Section 3, we demonstrate our detailed procedures of mapping the material property space of the CMMs step-by-step, check whether our explored property space is a full closure that contains all possible combinations of structural properties, and quantify uncertainty in property space associated with the surface distortion. Results of our explored material property space with deterministic and stochastic properties are provided in Section 3 as well. Section 4 discusses possible applications and future works of our mapping framework. Section 5 is the conclusion. To summarize, the contributions of this work are listed below:

- Select the CMMs among their families by comparing their mechanical properties in a compact way.
- Increase the applicability of the ML models for inverse design problems of the CMMs by referring to a maximal material-property space.
- Visualize the effects of manufacturing defects on the mechanical performance of the CMMs intuitively through various regions in the material-property space.

Part 1: Mapping a material-property space



Part 2: Uncertainty quantification

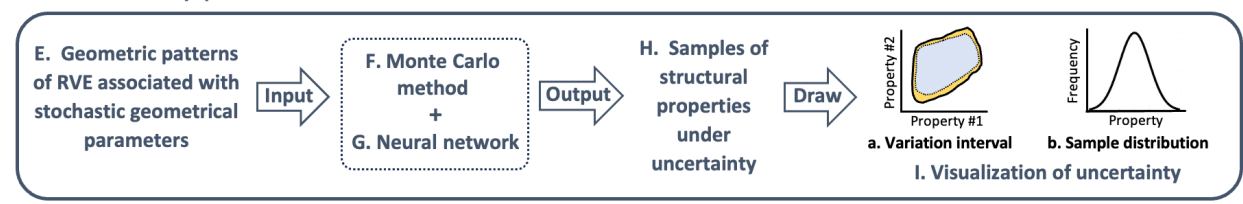


Fig. 1: Schematics of the presented procedures to map a material-property space under uncertainty (GA algorithm figure courtesy of [29]).

2. Methodology

2.1. Definition of Geometric Patterns

To demonstrate our framework, this study focuses on mapping the material-property space of a special but widely used class of CMMs, 2D porous cellular solids with periodic RVEs. The mechanical properties of these CMMs depend on the geometry of the underlying unit cells, such as the shape of the pore as shown in Fig. 2. In unit cells of these CMMs, the contours of the pores are four-fold symmetrical and defined as [26]:

$$r(\theta) = r_o(1 + \zeta_1 \cos(4\theta) + \zeta_2 \cos(8\theta)) \tag{1}$$

$$r_o = L\sqrt{\frac{2\phi}{\pi(\zeta_1^2 + \zeta_2^2 + 2)}}\tag{2}$$

where θ is the polar angle with $0 \le \theta \le 2\pi$, r is the polar radius, L is the size of the unit cell, and φ is the porosity. The geometric parameters $\zeta = (\zeta_1, \zeta_2)$ determine the family of different porous shapes. Fig. 2 demonstrates several sample geometric patterns of unit cells with various pore shapes controlled by the parameters ζ . In this work, L and φ are fixed and equal to 10 mm and 0.45, respectively.

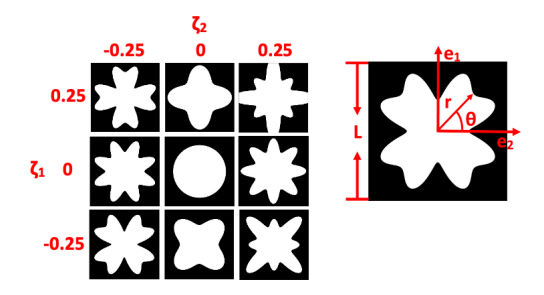


Fig. 2: Sample porous shapes generated by the formulations given in Eqs. 1 and 2.

The baseline geometry of this work is a representative volume element (RVE) with infills of unit cells described by the parameterization in Eq. 1 and 2, as illustrated in Fig. 3. A geometric pattern of the simplest RVE consisting of periodic unit cells (PUCs) is determined by two geometric parameters ζ_i (i = 1,2). As the number of identical cells in RVE becomes as large as $n \times n$, the number of geometric parameters ζ_i dramatically increases to $2 \times n \times n$, potentially leading to an increased level of randomness in geometric dimensions and corresponding properties of CMMs. Each pair of geometric parameters (ζ) controls the associated contour of the particular unit cell in the RVE. All geometric parameters are assigned in order as a geometric matrix shown in Fig. 3. In this work, two particular families of the CMMs are investigated to perform the material selection through the comparison of their material-property spaces shown in the discussion. Besides, this work chose 2×2 unit cells for mapping a material-property space of CMMs under uncertainty to balance the number of geometric parameters and the availability of computational power.

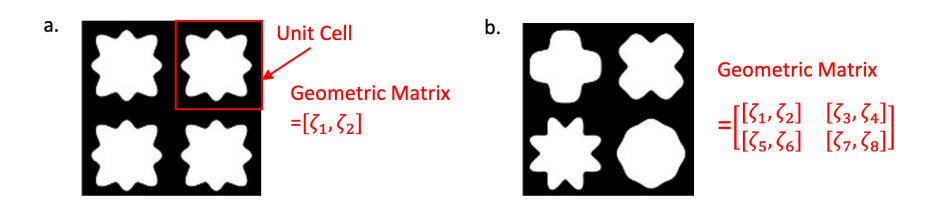


Fig. 3: Representative volume elements (RVEs) of the CMMs with (a) PUCs and (b) non-PUCs.

2.2. Computation of Elastic Properties

In the scope of linear elastic materials, the RVE homogenization method is applied to evaluate the equivalent constitutive mechanical behavior of periodically patterned microstructures (geometric patterns of RVEs), called effective structural properties. This work focuses on two of the most attractive structural properties of the CMMs in the recent study, Young's modulus and Poisson's ratio [30, 31, 32, 33]. Combinations of these two properties are illustrated as property points distributed in a 2D material-property chart (Fig. 1D). Each single UC and RVES with PUCs may demonstrate isotropic properties due to the four-fold symmetry of UCs. However, the homogenized properties of 2D RVEs of non-PUCs are anisotropic due to the non-periodical assignments of UCs within the given RVE, which expands the property space of RVEs significantly. For the consistency of our numerical cases, this work mainly explores the property space containing combinations of effective Young's modulus (E_{11}) and Poisson's ratio (v_{12}) of the CMMs, which are determined by applying strain tests in a longitudinal direction on a fine-mesh finite element model shown in Fig. 4. This study employs an open-source Abaqus plugin called EasyPBC [34] to estimate the homogenized effective elastic properties of periodic RVEs of the CMMs. The EasyPBC automatically defines the periodic boundary conditions, loads, and interactions in a meshed finite element (FE) model of RVEs. In Abaqus, the FE simulation is performed based on the homogenization method which requires numerically imposing uniform strains (Fig. 4) on several independent sets of RVE's surface to calculate specific elastic material properties [34]. The calculation of the two effective properties $(E_{11} \text{ and } v_{12})$ is performed in an Abaqus–Python environment by using the equations defined in Eqs. 3 and 4 [34]:

$$E_{11} = \frac{\text{Axial Tensile}}{\text{Axial strain}} = \frac{\sum F_{nodal} / A_{front}}{\triangle W / W}$$
(3)

$$v_{12} = \frac{-\text{Transverse strain}}{\text{Axial strain}} = \frac{\triangle H/H}{\triangle W/W}$$
 (4)

where F_{nodal} is the nodal force applied on sets of points on the boundary of the RVE, A_{front} is the front surface area which is equal to the height (H) of the RVE x unit thickness in 2D case, and W is the width of the RVE.

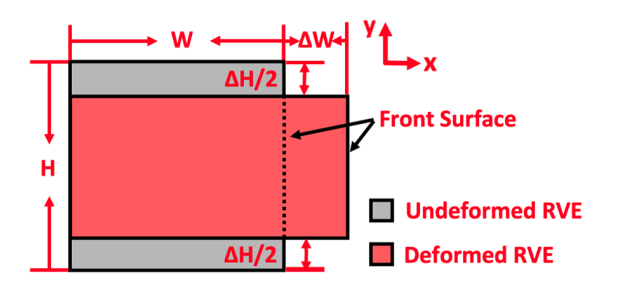


Fig. 4: Deformation of the RVE under uniform strain test in a longitudinal direction.

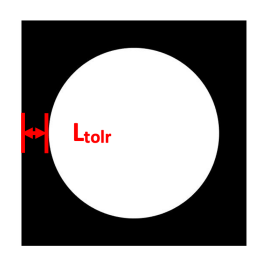


Fig. 5: Geometric Constraint.

2.3. Sampling Method by Genetic Algorithm

In material design problems, the genetic algorithm (GA) is commonly employed as an optimization method to retrieve optimal geometric patterns with the same or similar structural properties as given objective properties [22, 23, 24]. Instead, this work employs the genetic algorithm (GA) as a sample algorithm to exercise geometry-property models over a microstructure hull consisting of all possible geometric patterns of the RVEs. During the stochastic searching process, our mapping framework is interested in collecting all individuals of the GA rather than its optimal solutions. Each collected individual has a unique combination of structural properties associated with their corresponding microstructures tailored by the GA. Their property information is represented as property points in a 2D material property chart. The uniqueness of property points avoids redundant information for space determination. The information contains their distributed density and locations in the chart. In our GA solution, the individuals are produced by uniform crossover with a prescribed crossover rate. With the uniform crossover, each geometric parameter of reproduced individuals is randomly selected from one of the corresponding parameters of the parent chromosomes

[35]. Meanwhile, the uniform mutation increases the diversity of the individuals and enables the GA to perform more extensive exploration on microstructure hull (parameter space) of the CMMs. With the uniform mutation in the GA, each geometric parameter is randomly selected for mutation with a associated probability rate [36]. This probability rate is called the mutation rate and determines the probability of the selected parameters being mutated. After running the GA with the given objective properties, the framework collects the individuals with unique structural properties and scatters them into a material-property chart as property points. The bounded region of these property points (children of the GA) illustrates the explored material-property space during the stochastic searching process of the GA. Unlike the convex hull, this framework defines the region by using a built-in function in MATLAB called *boundary*, which can precisely envelop the points by shrinking towards the interior of the convex hull [37]. What's more, our GA solution is assigned with a high mutation rate (defined in Sec. 3) to increase the diversity of the individuals and provide better coverage of the microstructure hull [38, 39]. Consequently, it increases the diversity of property points, resulting in a high possibility of discovering a comprehensive property space based on their point distributions.

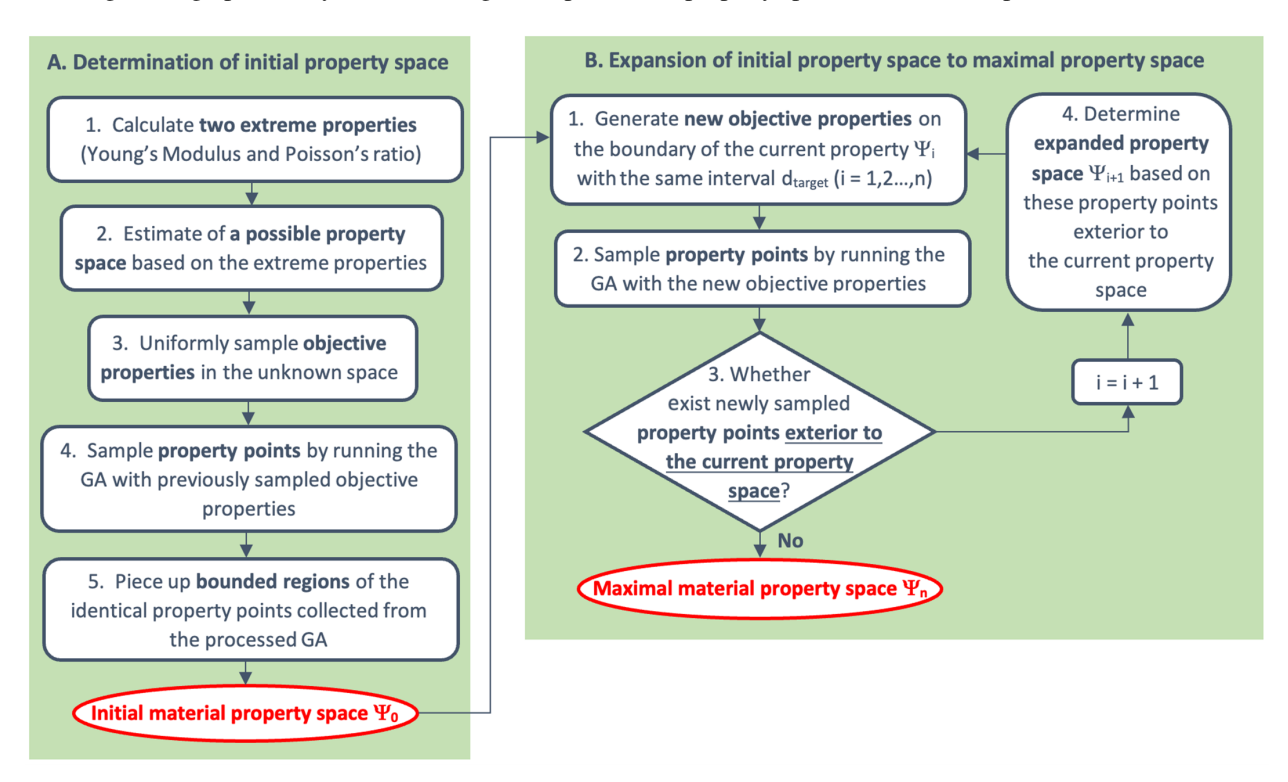


Fig. 6: Flowchart of sampling method including the selection of objective properties and the stochastic search algorithm of property points.

The sampling method of our mapping framework is summarized in a flowchart shown in Fig. 6. The first part of the method uses these property points as prior information to estimate an initial material-property space by piecing up the bounded regions corresponding to various objective properties (Fig. 6A). To choose the objective properties, the method first determines the extreme values of structural properties under consideration, Young's modulus and Poisson's ratio (Fig. 6A-1), and then roughly estimates a possible material property space (Fig. 6A-2) with a rectangle shape whose side length determined by the extreme values. After that, the objective properties are determined by uniform sampling (Fig. 6A-3) in this rectangular material property space. To precisely estimate the initial material property space of the CMMs, the GA processes the stochastic search algorithm (Fig. 6A-4) to check whether the sampled objective properties are within the actual property space of the CMMs. Consequently, an initial material property space can be determined by the overall space region covered by the convex hulls in a 2D material-property chart (Fig. 6A-5). To maximize the region of the initial property space, the second part of the method selects new

objective properties on the explored space boundary to push the newly generated geometric patterns from the GA past the current boundary (Fig. 6B). It applies a similar sampling algorithm as the first part but with a different selection method of objective properties (Fig. 6B-1). The objective properties are selected on the space boundary, which induces the stochastic search algorithm to generate property points that bypass the current boundary (Fig. 6B-2). The algorithm progressively expands the property space (Fig. 6B-4) to be maximal until none of the newly generated property points are located outside the current explored space (Fig. 6B-3). To validate the maximal region of the explored property space, new objective properties are generated nearby and beyond the space. These objective properties attempt to force the GA to search unexplored property spaces that might contain a new combination of properties, which can be physically achieved by undiscovered geometric patterns of the RVEs in the microstructure hull. After a new round of the stochastic searching process, the users can approximate its region to be maximal if none of the children or property points locates exterior to the current maximal space.

The basic idea of sampling the property points is to solve the inverse design problem of CMMs by the GA. This work formulates the inverse problem into a combined objective optimization problem that aims to minimize the difference between the objective properties and predicted structural properties of the RVEs. By minimizing the difference, the objective properties guide the GA to sample property points nearby desired locations, which could help to define an initial property space or to bypass the explored property space. In this work, the objective properties are the two structural properties of CMMs, Young's modulus and Poisson's ratio. The mathematical formulation of the inverse problem reads as follows [24]:

Minimize:
$$f(\zeta_{1}, \zeta_{2}, ..., \zeta_{n}) = [w_{1}(v_{12} - v_{0})]^{2} + [w_{2}(E_{11} - E_{0})]^{2}$$

Find: $\zeta = (\zeta_{1}, \zeta_{2}, ..., \zeta_{n})$
Subject to: $\zeta^{L} \leq \zeta_{i} \leq \zeta^{U}(i = 1, 2, ..., n)$
 $rsin(\theta) + L_{tolr} \leq \frac{L_{o}}{2}, rcos(\theta) + L_{tolr} \leq \frac{L_{o}}{2}$ (5)

where $\zeta = (\zeta_1, \zeta_2, ..., \zeta_n)$ denotes the vector of design variables and geometric parameters of the CMMs. ζ^L and ζ^U are the lower and upper bounds of the design variables, respectively, and w is a weighted coefficient to rescale the two effective properties in the same numerical level. v_0 and E_0 are the objective Poisson's ratio and Young's modulus of the GA, respectively. In this work, the poor simulation results from ABAQUS are mainly contributed by failures to generate feasible geometric patterns of the RVEs. For example, internal pore shapes beyond the RVEs lead to bad connectivity of the structures. Moreover, thin connections between the four symmetrical parts cause a large chance of structural failures under a small strain value. To avoid the above issues, the geometric constraint is assigned as shown in Fig. 5. In the constraint, the smallest distance between the boundary of the pore and the edge of its unit cell should be larger than a length tolerance, $L_{tolr} = 1$ mm. If the geometric patterns violate the constraint, the value of the objective function is appended with a penalty value, which is determined based on the level of magnitude of the objective value.

2.4. Deep Learning Model

To determine the uncertainty of structural properties due to the stochastic design parameters, a straightforward approach is to use the Monte Carlo (MC) method. As the number of samples increases, the number of forecasts also grows to allow the occurrence probability of each outcome to be estimated with better accuracy. Substantive and iterative simulations in the MC method result in a very high computational cost due to the expensive finite element analysis in the RVE homogenization. As mentioned in the introduction, the slight variations in the geometric parameters enable us to approximate surface distortion during the cooling process of the FFF/FDM demonstrated in Sec. 3.3. With this feature, the surface distortion in our study is approximately parameterized by the geometric parameters of the CMMs (See Sec. 2.1). Therefore, to accelerate the MC sampling, we can build a surrogate model with inputs of the geometric parameters to bypass the expensive finite element (FE) simulations and accelerate the MC sampling. In a forward fashion, the deep learning approach provides accurate predictions for structural properties of RVEs at a relatively low computational cost compared to the FE simulations. In this study, a surrogate model is built as a connected multi-layer neural network called a Multilayer Perceptron. Its hidden layers are made up of a set of neurons with parameter sets (ω) containing the weights and biases. In the neural network, the geometric parameters (ζ) are mapped onto their two structural properties, E and ν , in a forward fashion. The objective of training the surrogate model of neural network (NN) is to minimize the loss between actual values and predictions concerning the

NN parameters, ω . The performance of NN is evaluated in terms of the mean squared error and is defined in Eq. 6 [40]:

$$\min_{\omega} MSE = \frac{1}{n} \sum_{i=1}^{n} (y_i - \hat{y}_i)^2$$
 (6)

where y_i is the actual property of CMMs, and $\hat{y_i}$ is the property predicted by the trained surrogate model. For uncertainty quantification of the space, the deep learning approach assists Monte Carlo simulation by effectively generating a set of varying properties corresponding to an estimated range of values, as opposed to using deterministic design variables.

3. Results

This section presents the numerical results of two families of the CMMs, the RVEs with periodical unit cells (PUCs) and with non-periodical unit cells (non-PUCs). The framework includes four main steps: (i) discovering the initial mechanical property chart, (ii) expanding the incomplete material-property space, (iii) validating the converged material-property space to be maximal, and (iv) uncertainty quantification in the maximal property space. Here, a case study of RVEs with PUCs demonstrates the detailed procedures of our proposed sampling algorithm for the determination and validation of maximal material-property space. By considering their complex geometric patterns, a case study of RVEs with non-PUCs illustrates the uncertainty quantification of its maximal property space. In these study cases, the base material of the RVE is chosen as ULTEM® 1000, an amber transparent high-performance polyetherimide (PEI) with isotropic elastic properties, i.e., Young's Modulus of 3580 MPa and Poisson's ratio of 0.36 at room temperature [41]. For all the study cases, the basic settings of the GA are almost the same to check the compatibility of our sampling algorithm. The same settings of the GA include the stall generation limits, crossover rate, and function tolerance of GA, which are set to 16, 0.8, and 10⁻⁶, respectively. However, the population size and maximum iteration number vary according to specified factors, such as the number of geometry parameters, locations of selected objective properties, and certain procedures of the sampling algorithm (See details in Sec. 3.1). In addition, the mutation rate is defined as 0.01 to obtain extreme properties in Fig. 6A-1 by solving the optimization problem with a standard GA. The sampling property in Fig. 6A-4 and B-2 requires the GA with a high mutation rate of 0.8 which promotes more exploration in microstructure hulls. For each objective property, their stochastic search process will be terminated when the relative change in the best fitness function value over the maximum stall generation is less than the tolerance, or the maximum generation number is reached. The major numerical results are illustrated in the following subsections, including convergence histories of material-property spaces of the two families (Figs. 11 and 15), maximal/converged material-property spaces of them (Figs. 12 and 16), satisfactory convergence behavior of structural properties of RVEs with non-PUCs (Fig. 19), the performance of a well-trained neural network for accelerating the MC method (Fig. 23), and variations in the properties and space boundary (Fig. 24).

3.1. Estimation of Material Property Space of RVEs with PUCs

Following the sampling algorithm in Fig. 7, our proposed framework explores the material-property space of the simplest RVE consisting of periodic unit cells, whose geometric patterns are only controlled by two parameters ζ_i (i = 1,2) shown in Fig. 3a. Initially, there is no prior information about the actual property space, consisting of possible property points that can be physically realized by tailoring geometry patterns of the RVEs. Instead of random sampling in RVEs without clues, our framework processes the GA as a sampling algorithm with the objective properties achieved by uniform sampling in a possible property space. The possible property space is a rectangle-shaped region whose side lengths depend on values of extreme structural properties. The framework employs the GA to determine the extreme properties to avoid local convergence in the optimization process due to the complex parameter domain shown in Fig. 7a [42]. In this case, the objective function in Eq. 5 is replaced by E_{11} or v_{12} for the minimization and $-E_{11}$ or $-v_{12}$ for the maximization with the same constraint. Given the population size defined as 32 and the maximum iteration number defined as 150, the ranges of Young's modulus and Poisson's ratio are estimated by the GA, which are [704.62, 1284.58] MPa and [0.1074, 0.1939], respectively. To standardize the data and make it easy to analyze, structural properties generated by the current and following steps of the expansion process are all normalized using their extreme values determined in the current step.

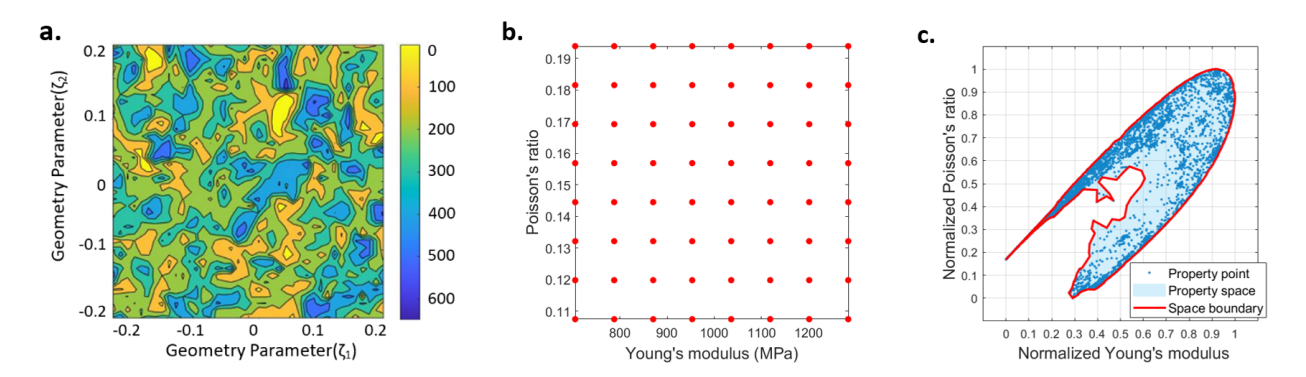


Fig. 7: Determination of initial material-property space: (a) contour of objective values in 2D parameter space, (b) uniform sampling of objective properties in a possible property space, and (c) initial material-property space (normalized).

In Fig 7b, 64 property points are uniformly sampled in this rectangular-shaped property space and are defined as objective properties of the GA. The stochastic search process samples property points surrounding these objective properties and checks whether the objective properties are located in the actual property space. Thus, this framework applies GA not only to estimate the region of the material-property space in longitudinal and transverse directions based on the extreme properties but also to estimate the region from all other possible directions. For the sampling purpose, the population size is reduced to 16, with the maximum iteration number defined as 100 in Step A-4 (Fig. 6). It also helps to reduce the computational cost. The average errors obtained by the experiments between the objective and predicted properties are 0.45% and 0.47% for Young's modulus and Poisson's ratio, respectively. These errors are acceptable because the primary purpose is not achieving the global optimum. During the overall sampling process, we only collect property points with unique combinations of two structural properties to avoid redundant information for space determination. Consequently, 6406 property points are collected and denoted as blue dots in Fig. 7c. Ultimately, the initial material-property space is determined by piecing up the bounded region of these property points or the explored spaces of each run of the GA. Fig. 7c shows the initial material-property space (denoted as a light blue region) illustrated by a normalized material-property chart, whose longitudinal and transverse axes are assigned with Young's modulus and Poisson's ratio, respectively. The region of the space is defined by its boundary, denoted as a red solid line in Fig. 7c.

However, the initial property space shown in Fig. 7c is incomplete and fails to cover all possible combinations of structural properties. To this end, this work introduces an intuitive approach to expand the space region to the maximum progressively. This approach begins with selecting 66 new objective properties on the boundary of the initial property space, denoted as blue dots in Fig. 8a. Two neighboring objective properties have the same interval, or the shortest Euclidean distance between them, $d_{target} = 0.06$ shown in Fig. 8a. Since the expansion process intends to discover property points (children) located exterior to the current space region, this framework selects objective properties on the boundary instead of these selected within the space due to the distribution characteristics of the GA's children. After processing the 66 runs of the GA, the sampling algorithm generates 8801 new property points in total. In Fig. 8b, all the points are scattered on the initial material-property chart. They are denoted as the blue and orange points, representing the properties within and beyond the initial space, respectively. To expand the initial space, the framework is only interested in the non-overlapping regions between the bounded region of the newly generated points and the initial property space. The non-overlapping region is the newly expanded region of the property space. By combining the region with the initial property space, a newly expanded material-property space is achieved with enriched property points. Fig. 8c compares the regions between the newly expanded and initial property spaces, bounded by a dashed orange line and a solid blue line, respectively.

Following the iterative loop in Fig. 6B, this framework continues to expand the material-property space by using the sampling algorithm. In the study case, each iterative loop requires processing a large number of stochastic search processes corresponding to numerous objective properties selected on the boundary. With computationally expensive simulations in ABAQUS, the execution time of the single loop is enormous. To increase the computation efficiency of

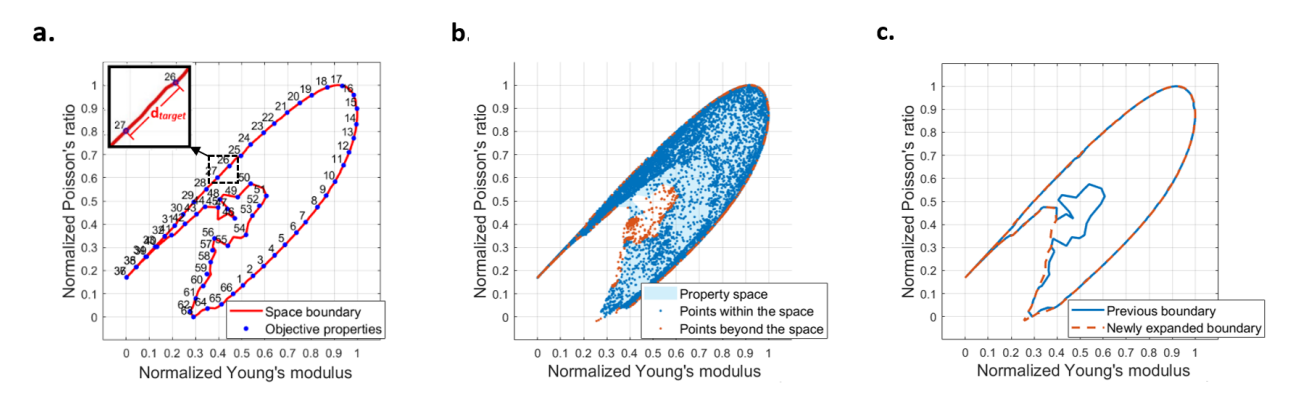


Fig. 8: The first expansion loop: (a) objective properties selected on the boundary of the initial property space, (b) distribution of all newly generated property points, and (c) comparison between the previous and the newly expanded boundary of the property space.

Table 1: Results of the GA with the sample violated objective properties.

Objective properties #	# Generations in total	Generation # (violated)
1	56	2, 5, 13, 14, 22
4	45	2
13	52	1, 4
19	50	21, 22
24	48	6, 14, 16, 18, 22
28	62	13
34	52	2, 11, 12, 13, 14, 17
37	47	2, 6, 10
52	46	1
58	46	12, 13

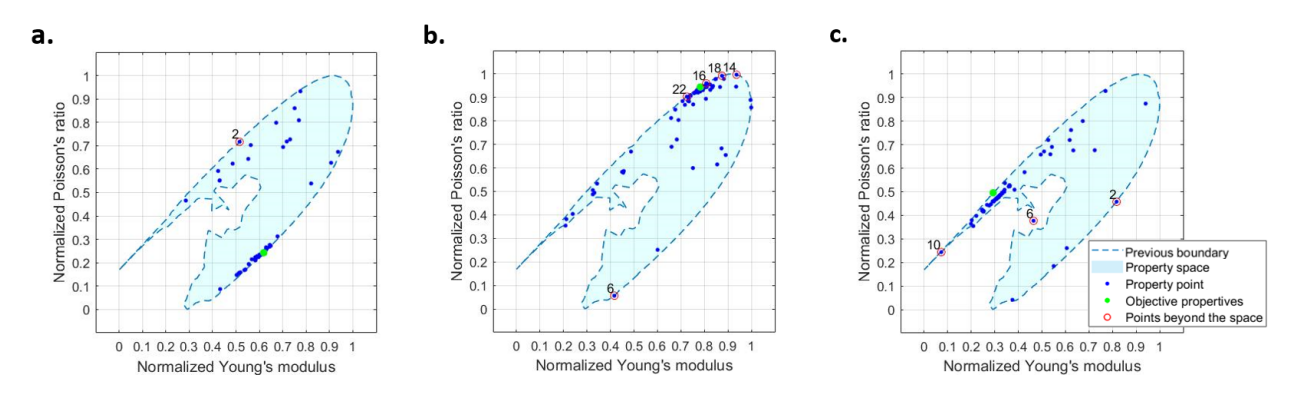


Fig. 9: Distribution of possible solutions of the sample violated objective properties with the indexes (a) #4, (b) #24, and (c) #37 from Table 1.

this iterative search process, this work studies the factors that increase the possibility of discovering property points exterior to the space. After several experiments, their results indicate that newly generated property points exterior to the space tend to appear in the first few generations of the GA if its objective properties selected on a newly expanded boundary (bounded by a dashed orange line in Fig. 8c) are close to the boundary determined from the

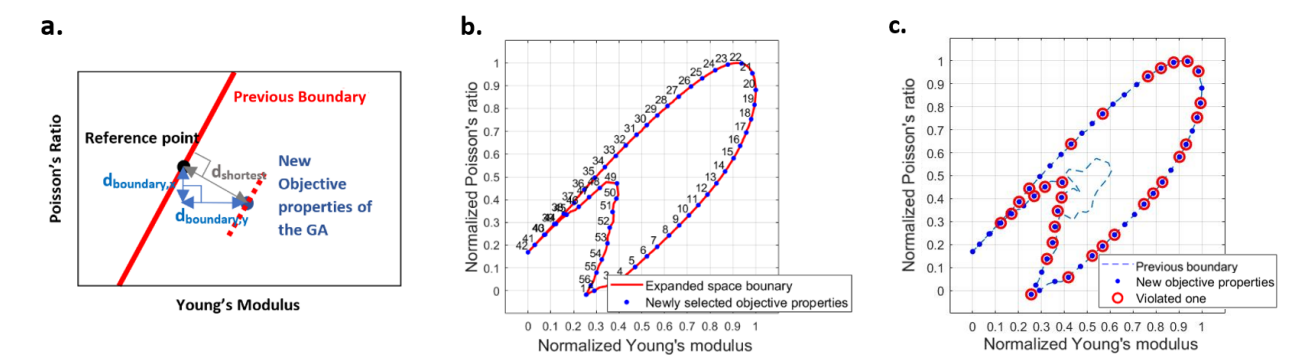


Fig. 10: Distance constraint applied in the second expansion loop: (a) Evaluation of distance from new objective properties to the previous boundary, (b) objective properties selected on the newly expanded boundary determined in the first expansion loop, and (c) violated objective properties circled in red.

previous loop/step (bounded by a solid blue line in Fig. 8c). Table 1 summarizes the experimental results of sample objective properties, which are close to the previous boundary. It summarizes the GA results, including the total number of generations and the indexes of the generations where the property points are located outside the newly expanded space. The experimental results can be visualized in Fig. 9, which illustrates the distribution of property points for three sample objective properties from Table 1. To assess how far the objective properties are from the previous boundary, this framework calculates the shortest Euclidean distance, $d_{shortest}$, from the objective properties to the previous boundary. The distance is determined in both longitudinal and transverse directions. In a normalized space shown in Fig. 10a, the horizontal and vertical distances of $d_{shortest}$ are denoted as $d_{boundary,y}$, respectively. Consequently, the distance constraint is defined as:

$$d_{boundary,x} \ge 0.05 \tag{7}$$

$$d_{boundary,y} \ge 0.05 \tag{8}$$

The distance constraint is violated, or the objective properties are close to the previous boundary if $d_{boundary,x}$ and $d_{boundary,y}$ of the objective properties are both less than 5% of the normalized ranges of two properties. The range is equal to one since it is defined by extreme properties from step A-1 (Fig. 6). The distance constraint begins to apply in the second expansion loop. In this loop, 56 new objective properties are selected on the newly expanded space boundary (Fig. 10b). Among these, 29 objective properties violate the distance constraints. They are processed in the GA with the reduced maximum iteration number. The violated objective properties are circled in red, shown in Fig. 10c. From Table 1, the maximum iteration number can be significantly reduced from 150 to 25. In the section on numerical results, this framework employs the same distance constraint and reduced maximum iteration number for the following expansion loops of both RVEs with PUCs and non-PUCs.

After three expansion loops, the material-property space converges. In the fourth expansion, none of the newly generated property points is exterior to the previous space boundary. In Table 2, the number of violated objective properties is the same as the number of objective properties selected on the space boundary determined in the fourth expansion. It indicates the space barely or doesn't expand the space in the last expansion loop, which also implies the convergence of the space. The numerical results of the whole space exploration process are summarized in Table 2. It contains the number of total objective properties, violated objective properties, and newly generated property points in each step. Convergence histories of the normalized space boundary and space area are shown in Fig. 11a and Fig. 11b, respectively. In summary, 29113 property points are produced through the whole space exploration process, denoted as blue dots in the converged property space shown in Fig. 12.

In the post-process, to validate that the converged property space is maximal, 62 new objective properties with the same shortest Euclidean distance from its boundary, $d_{validation} = 0.03$, are generated in an outward direction that is normal to the final normalized space boundary and picked in Fig. 13a. We assumed that the GA has the capability of creating several possible property points that approach these new objective properties and proves that these objective

properties are achievable and within the actual property space. By considering that the number and diversity of the children might restrict the expansion of the material-property space, the population size and the maximum iteration number are increased to 32 and 150, respectively. However, after running the GA, all new 6669 property points cluster nearby the boundary of the converged property space in Fig. 13b and cannot bypass the boundary. It indicates that the assumption is invalid. Thus, the converged material-property space of RVE with PUCs is validated, which has the maximal space region that covers all possible combinations of Young's modulus and Poisson's ratio as shown in Fig. 12.

Table 2: Summary of the whole space exploration process of the CMMs with PUCs.

Step #	# Objective properties (total)	# Objective properties (violated)	# Property points
0	64	-	6404
1	66	0	8801
2	56	29	5609
3	57	45	4400
4	57	57	3899

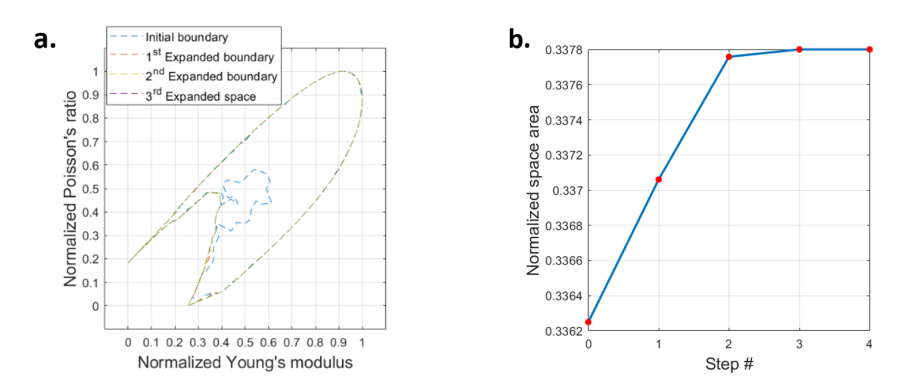


Fig. 11: Convergence histories of (a) the normalized property space boundary and (b) space area.

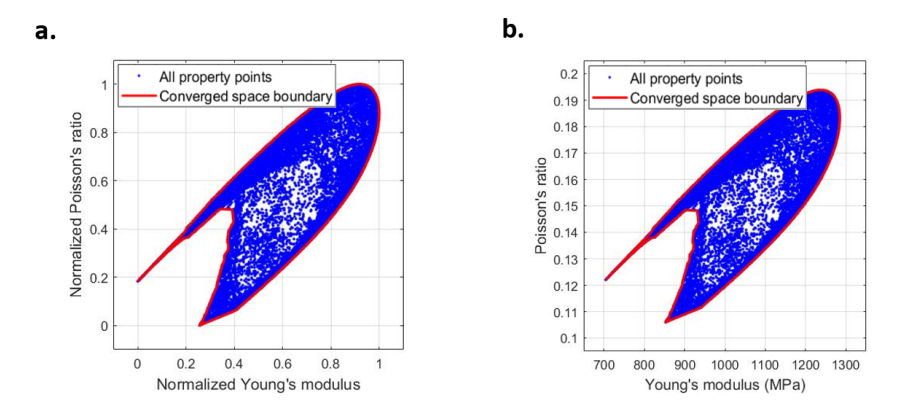
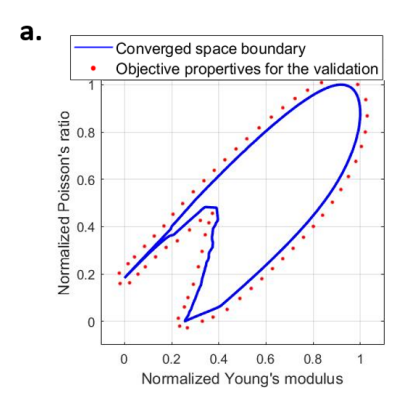


Fig. 12: Converged property space: (a) the normalized space and (b) the original space.



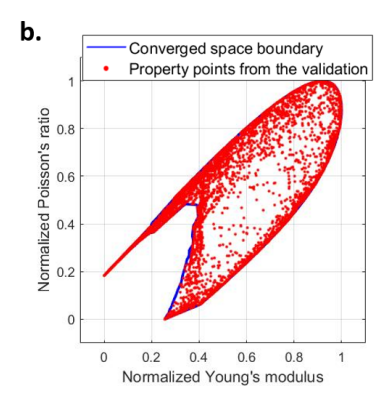


Fig. 13: Post process of the space exploration: (a) objective properties for the validation and (b) newly generated property points from the validation.

3.2. Estimation of Material Property Space of RVEs with Non-PUCs

The framework is also applied to explore the material property space of CMMs with non-PUCs, whose geometric patterns are controlled by a geometric matrix containing eight geometric parameters $[\zeta_1, \zeta_2, \zeta_3, \zeta_4, \zeta_5, \zeta_6, \zeta_7, \zeta_8]$ shown in Fig. 3b. Following the same exploration procedure shown in Fig. 6, the extreme properties are first determined by the GA. Compared with the parameter space in the previous study case, its dimension in this study case increases from 2D to 8D due to increases in the complexity of geometry patterns of the RVEs. In a high-dimensional parameter space, premature convergence is more likely to appear during the stochastic searching process. To maintain the performance of the GA, the population size and the maximum iteration number are increased to 64 and 250, respectively. With these settings of the GA, the longitudinal and transverse bounds of the property space are determined as $E \in [731.42,$ 1244.40] MPa and $\nu \in [0.0904, 0.2153]$ MPa. Once the rectangular-shaped possible property space is defined, this framework uniformly samples 64 objective properties in the space, illustrated in Fig. 14a. For exploring an initial property space, these objective properties are applied to sample property points of the CMM with non-PUCs, which contain combinations of properties that can physically be realized by their corresponding geometric patterns of the RVEs. For the sampling algorithm, the new population size and maximum iteration number are defined as 32 and 150, respectively. It allows the framework to discover 21481 property points. The average errors for Young's modulus and Poisson's ratio are 0.41% and 0.48%, which are assumed to be in acceptable ranges for sampling purposes. In Fig. 14b, the initial property space is achieved by combining the bounded regions of these sampled points.

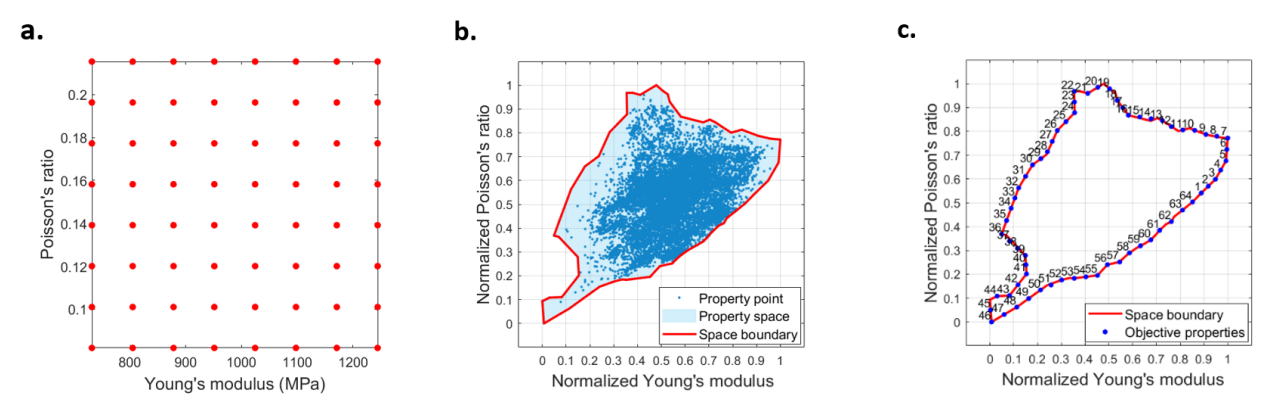


Fig. 14: Determination of the material-property space: (a) uniform sampling of objective properties in a possible property space, (b) initial material-property space (normalized), and (c) objective properties selected on the space boundary.

Table 3: Summary of the whole space exploration process of the CMMs with non-PUCs.

Step #	# Objective properties (total)	# Objective properties (violated)	# Property points
0	64	-	21481
1	64	0	14703
2	57	8	12605
3	52	26	8851
4	50	29	8240
5	52	33	8005
6	50	33	7883
7	50	38	6442
8	50	47	3564
9	50	50	2432

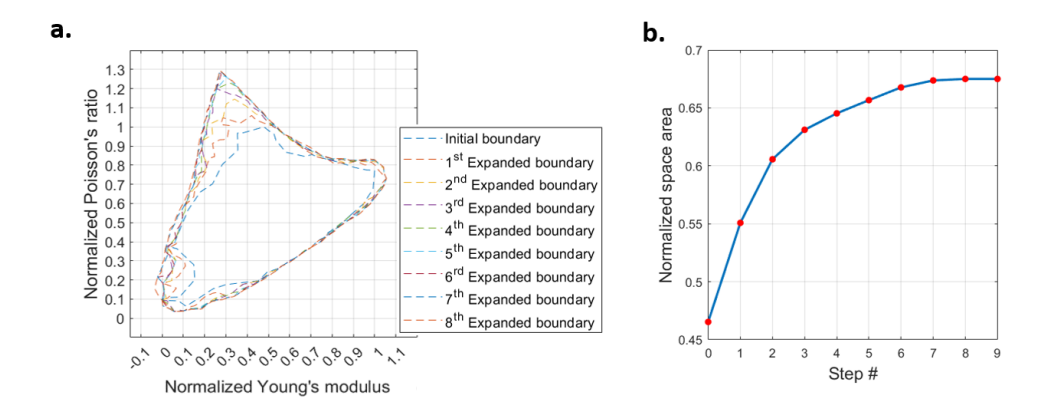


Fig. 15: Convergence histories of (a) the normalized property space boundary and (b) space area.

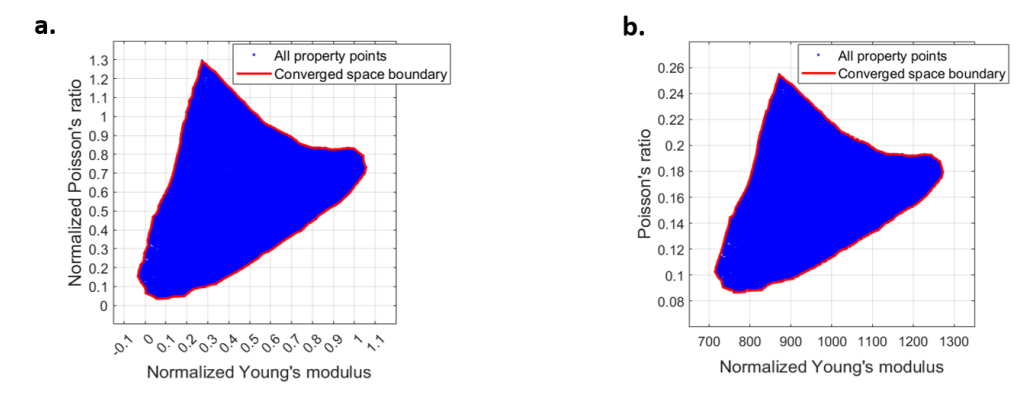


Fig. 16: Converged property space: (a) the normalized space and (b) the original space.

To check the compatibility of the framework, the settings of the following iterative expansion loops are the same as in the previous study case. The settings include $d_{target} = 0.06$ for selecting the objective properties on the boundary (Fig. 14c) and tolerance = 0.05 for defining the distance constraint. The property space eventually converges after expanding the space region eight times. Convergence histories of the normalized space boundary and space area are shown in Figs. 15a and 15b, respectively. Combined with property points in estimating initial property space, 94206

unique combinations of Young's modulus and Poisson's ratio are densely scattered in the converged space during the whole space exploration process of the CMMs with non-PUCs (Figs. 16a and 16b). Table 3 summarizes the numerical results of the whole process. In Fig. 15a, it is noticed that the longitudinal and transverse bounds of the property space significantly enlarge, as well as the bounds in the other directions. From Fig. 16b, the extreme values of Young's modulus and Poisson's ratio increase to [717.37, 1272.83] MPa and [0.0867, 0.2547], respectively.

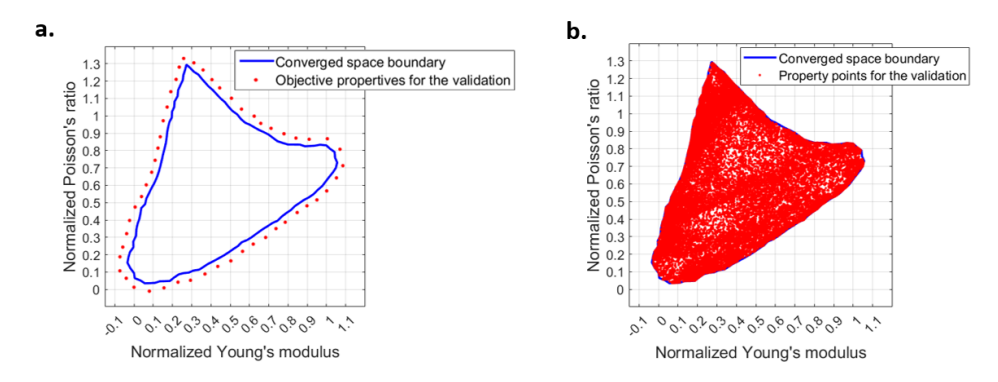


Fig. 17: Post process of the space exploration: (a) objective properties for the validation and (b) newly generated property points from the validation.

Besides, the converged property space is required to be validated as the maximal space. With $d_{validation} = 0.03$, 52 new objectives properties are picked nearby its converged boundary for processing the validation step (Fig. 17a). Considering the expansion limits caused by the limited diversity and quantity of the property points, the population size and the maximum iteration number increase to 64 and 250, respectively. After all, in Fig. 17b, none of the new 34893 property points in the validation step can bypass the converged boundary and only infinitely approach the boundary. Thus, the converged property space (Fig. 16) is successfully validated as the maximal space.

3.3. Uncertainty Quantification (UQ) in Property Space

Considering structural complexity, this paper aims to quantify the uncertainty in the material-property space of the RVEs with non-PUCs. Here, the uncertainty of properties is mainly induced by surface distortion in fused filament fabrication (FFF) [43]. For FFF-printed polymer parts, the defect appears due to uneven thermal shrinkage from their poor heat conduction and residual stress from their various thicknesses [44, 45]. This study simulates the manufacturing defect by varying the porous shapes within RVEs. To simplify this simulation, this study characterizes the variation by eight geometric parameters from the geometric matrix shown in Fig. 3b. As illustrated in Fig. 18, a minor change in the parameter values allows for slight expansion and shrinkage in the porous shapes from different polar angles (θ in Eq. 1). By referring to tolerances in FFF printing [44, 46], the uncertainty levels of the geometric parameters are specified in three tolerance cases: $d\zeta_i \sim U(-10\%, +10\%)$, $d\zeta_i \sim U(-20\%, +20\%)$, and $d\zeta_i \sim U(-30\%, +30\%)$. With the fixed side length of the RVEs L=10mm, the tolerances of polar radius (r) are ± 0.09 mm, ± 0.19 mm, and ± 0.28 mm corresponding to these three tolerance cases.

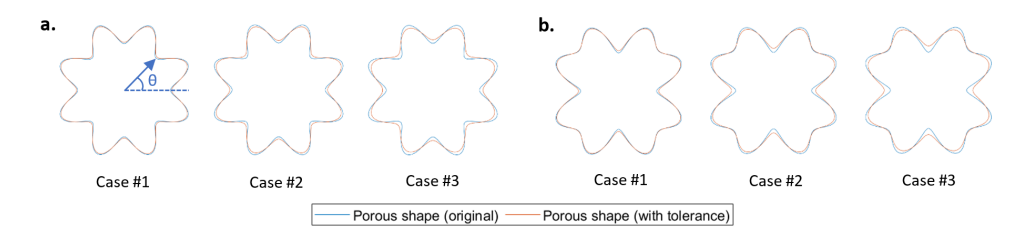


Fig. 18: Variations in the porous shapes with three tolerance cases (+10%, +20%, 30%): (a) $[\zeta_1, \zeta_2] = [0.01089, -0.2012]$ (b) $[\zeta_1, \zeta_2] = [-0.1598, -0.1797]$.

Due to its simplicity and high dimensional stochastic design space with eight geometric parameters (Fig. 3b), the Monte Carlo (MC) method is utilized to quantify various outcomes for structural properties under the effects of uncertainty arising from manufacturing defects [47]. In Fig. 19a and 19b, after 50,000 MC iterations, satisfactory convergence behavior is obtained for the first (mean, m_1), second (standard deviation, m_2), third (kurtosis, m_3), and fourth (skewness, m_4) statistical moments for both Young's modulus and Poisson's ratio. The distribution histograms of the two properties shown in Fig. 19c suggest that the two properties can be approximately considered as normally distributed random variables. In Fig. 19c, the geometry constraint induces the lack of samples of Young's modulus in the left tail of its histogram. Based on the satisfactory convergence behavior, our study processes MC sampling with 50,000 samples for 120 representative property points selected on the maximal space boundary (Fig. 21). These property points represent the contour of the maximal space region and contain information on the deterministic geometry matrix consisting of eight geometric parameters. In the aforementioned three tolerance cases, the geometric matrix contains stochastic geometric parameters, which demonstrate uniform distributions and contribute to the variations in their geometric patterns. Consequently, the variations lead to uncertainties in the structural properties. The combination of these uncertainties alters the deterministic region of the maximal material-property space.

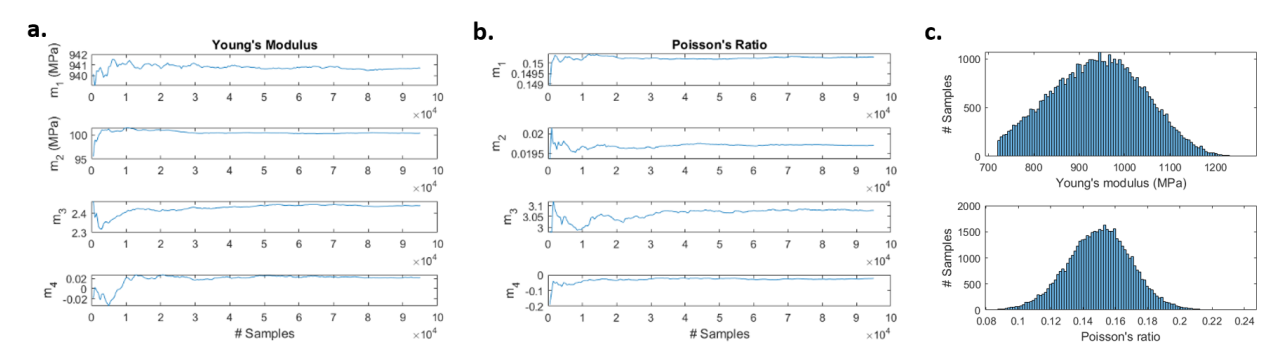


Fig. 19: Pre-processing of the MC method: (a) convergence histories of statistical moments for Young's modulus, (b) convergence histories of statistical moments for Poisson's ratio, and (c) distribution histograms of the two properties.

Here, the deep learning method is applied to accelerate the MC sampling. For numerous samples of the geometric parameters, it helps to predict the corresponding structural properties in a forward fashion efficiently. The database is built by collecting all the property points throughout the space expansion and validation process in Sec. 3.2. It consists of 129099 pairs of geometric matrices and their related properties, including Young's modulus (E) and Poisson's ratio (v). In the database, the property distribution is shown in Fig. 22a. However, the convergent behavior of the GA's children induces a specific pattern appearing in the distribution of samples from the database, such as the clusters with high sample density shown in Fig. 20b. It can introduce error or bias to the outcomes of an NN trained with this database. To prevent this potential issue, sample data in these clusters are partially eliminated to achieve dispersed distribution in the data domain (Fig. 20c). It is performed by evaluating sample density with Ripley's K-Function, a tool for analyzing point patterns in a 2D space [48]. After downsampling the samples in these clusters, the modified database remains with 73204 geometry-property pairs showing an approximate uniform distribution in Fig. 22b. This study splits the database into 80% of it for training and 20% for testing. Based on their extreme values, all data in the database are normalized to a common scale from 0 to 1. Our NN is devised into Multi-layer perception (MLP) architecture, constructed as two fully connected layers with 25 neurons (Fig. 23a). It is developed and tested using Keras with a TensorFlow backend and optimized in terms of the mean square error (MSE) metric. A regularization technique called early stopping is applied to prevent overfitting, which allows the training process to run for 37 epochs in total. The training process takes approximately 5.5 minutes on a single tensor processing unit version 3.0, which has 16GB of high-bandwidth memory pre-core. After the 37 epochs, the MSE is minimized to 1.7752e-04 and 1.7815e-04 for the training and validation datasets, respectively. Their small values and stable convergences (Fig. 23b) indicate the excellent capability of the NN to predict Young's modulus and Poisson's ratio as a function of user-defined design parameters. Furthermore, with 26684 samples from the test dataset, the capability can also be proved by showing the actual properties from the database and the predicted properties from the NN in the same plot. In Fig. 23c, a good fitness in the bisection line and narrow bandwidth of the scatter distribution validate the reliability of our NN. The good fitness can be numerically represented as the coefficient of determination (R^2) values of 0.9963 for E_{11} and 0.9973 for ν_{12} .

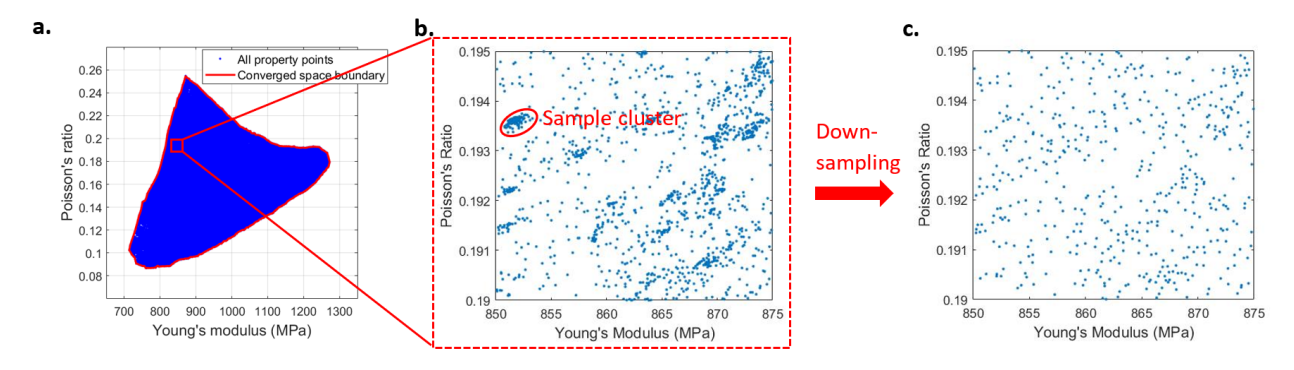


Fig. 20: Modification of the database: (a) the maximal material-property space, (b) detection of the clusters with high sample density, and (c) downsampling of samples in the detected clusters.

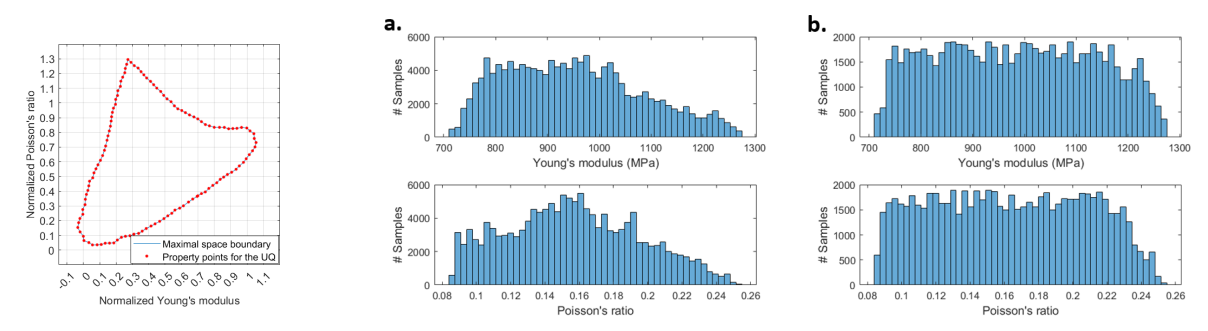


Fig. 21: Property points for the UQ.

Fig. 22: Distribution histograms of (a) original and (b) modified database.



Fig. 23: Deep learning method: (a) architecture of the NN, (b) convergence history of the MSE, and (c) comparisons between the actual and predicted properties.

Once the NN is well-trained, it can accelerate the MC sampling and efficiently predict structural properties associated with stochastic geometric parameters from three tolerance cases. To quantify the stochastic responses in the statistical sense, the mean values of two properties over the pre-defined uncertainty range and corresponding variances are obtained as follows:

$$\overline{P}(\zeta_i) = \frac{1}{N} \sum_{i=1}^{N} P_i(\zeta_i)$$
(9)

$$\sigma_P(\zeta_i) = \sqrt{\frac{\sum_{i=1}^N (P_i(\zeta_i) - \overline{P}(\zeta_i))^2}{N}}$$
(10)

where N is the size of MC samples, ζ_i is the geometric matrix of stochastic design parameters, and P denotes the structural properties under uncertainty. The 95% confidence interval of the structural properties under uncertainty can be determined as:

$$P_{95\%}(\zeta_i) = \overline{P}(\zeta_i) \pm 2\sigma_P(\zeta_i) \tag{11}$$

For the 120 selected property points, their mean values and corresponding variances are shown as 95% confidence intervals with error bars in Figs. 24a and 24b. By combining the interval regions of the two properties, the uncertainty in material-property space is determined. It can be visualized as variation intervals of the space boundary in the 2D material-property chart shown in Fig. 24c. Also, the uncertainty in combinations of two properties can be numerically represented as variations in the maximal space area shown in Table 4 with the three tolerance cases.

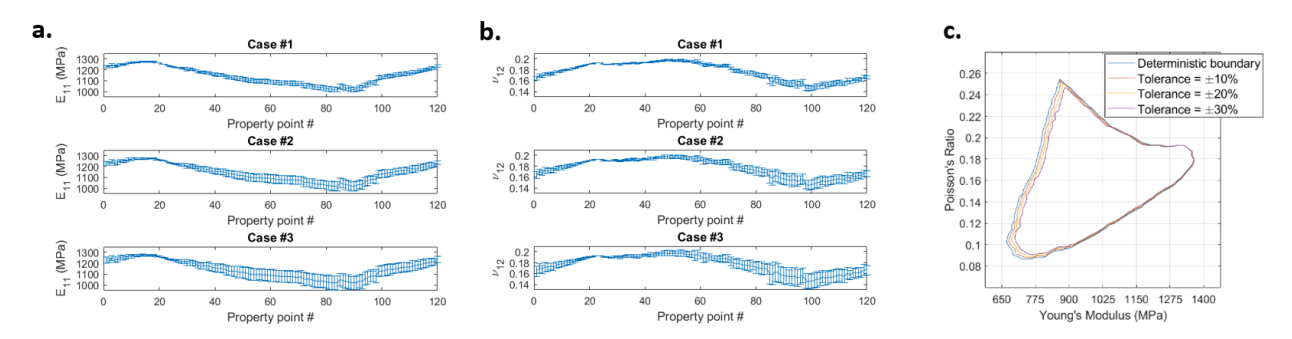


Fig. 24: Variations in properties associated with the three tolerance cases: (a) error bars for Young's modulus of all the property points for the UQ, (b) error bars for Poisson's ratio, and (c) variation intervals of the maximal space boundary

Table 4: Summary of normalized areas under the three tolerance cases.

	Case #0 (±0%)	Case #1 (±10%)	Case #2 (±20%)	Case #3 (±30%)
Normalized area	0.6750	0.6484	0.6228	0.5963

4. Discussion

The numerical results from the previous section demonstrate that our proposed methodology can precisely determine the maximal material-property space of the CMMs and effectively quantify uncertainty in the space area associated with the surface distortion. However, the major drawback of our methodology is the high computational expense of the whole exploration process due to the stochastic searching algorithm. For example, exploring and validating the property space of RVEs with PUCs requires the total number of selected objective properties to be as high as 362. These objective properties contribute to 362 runs of GA to process the sampling algorithm and complete the exploration process. Although time-consuming, our methodology is not content with a rough approximation of the property space with a small region and ends with a preliminary discovered property space in Fig. 7c and 14b. Instead, with the iterative searching algorithm, our methodology continuously expands the property space and approaches its maximum. Moreover, the mapping procedure is only required once for a specific type of metamaterials. Besides, we compare values of the calculated Hashin-Shtrikman (HS) bounds to the extreme values retrieved from the presented material property space boundary. The range of the calculated HS bounds for ν_{12} is [0.1521, 0.3172]. It cannot cover the range of effective Poisson's ratio obtained by the presented methodology, which is [0.0867, 0.2547]. The delicate design of geometric patterns of RVEs induces the minimum ν_{12} in material property space to fall beneath its lower HS

bound. Thus, the HS bound cannot provide an accurate range of Poisson's ratio. In addition, the work of Zimmerman et al. [49] declares that it is erroneous to determine the HS bounds of Poisson's ratio with the knowledge that shear and bulk moduli computations are erroneous. For this reason, the HS bound is not an appropriate choice for checking the limits of the selected material properties in this work. Besides, this section discusses possible applications of the presented material-property space exploration strategy, including the selection of materials among their families, assessment of the applicability of NN based on its data domain, and uncertainty quantification of multiple properties as a result of manufacturing defects. Our future works are summarized in this section as well.

4.1. Material Selection

In engineering design, material selection charts are a simple and quick way of initially screening materials for a particular application [50]. In this study, a material selection chart can be achieved by plotting all resulting materialproperty spaces obtained through our methodology in the same 2D material-property chart shown in Fig. 25. Our material selection chart has similar functions as Ashby's charts [51]. To assess materials' suitability for a given application, the chart screens out materials based on the coverage corresponding to their space regions in the same selection chart. In our study scenario, the space region of RVEs with non-PUCs (bounded with a blue line) is much more comprehensive than that of RVEs with PUCs (bounded with a green line) as illustrated in Fig. 25. For RVEs with non-PUC, the wide coverage of their space region is due to their complex geometric patterns containing various combinations of unit cells. In material applications, a narrow space region (RVEs with PUCs) requires trade-offs between two material properties to achieve users' requirements [50]. An expansive space (RVEs with non-PUCs) offers more options in combination with two properties. It allows its family of materials to have a broad application in engineering design. Moreover, in Fig. 25, the overlapping area of the charts (bounded with a red dotted line) provides alternative solutions in manufacturing processes. In this area, RVEs with PUCs share similar mechanical performance as RVEs with non-PUCs but possess simple geometric patterns of RVEs, which are easy to fabricate in manufacturing. Besides, in Ashby's chart, experimental data for each material family are clustered into multiple regions roughly shaped as bubbles [51]. With our methodology, the space region not only approximately reaches the maximal but is also precisely enveloped with a well-defined boundary. The boundary is initially determined based on a convex hull containing all the feasible property points from the exploration process. It can further shrink towards the hull's interior to represent the space region more precisely. It ensures the accuracy and reliability of material selection. To further proceed with the material selection process, the screening of materials can be followed by ranking the candidate materials using the analytical hierarchy process as the main Multi-Criteria Decision Making methodology for specific manufacturing processes [52].

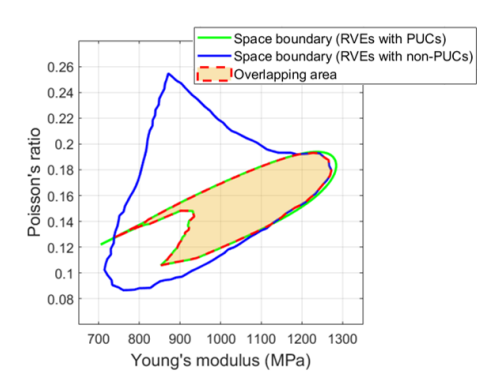


Fig. 25: Material selection chart of two families of the CMMs including RVEs with PUCs and RVEs with non-PUCs

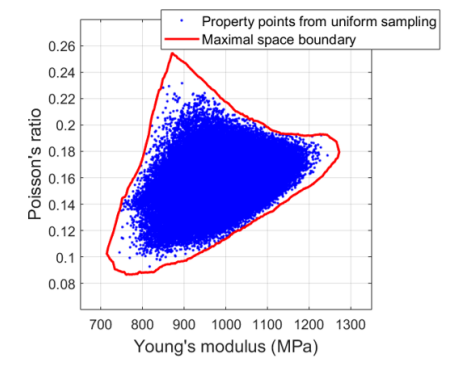


Fig. 26: Distribution of property points from the uniform sampling and the maximal material-property space boundary from Sec. 3.2

4.2. Applicability of Neural Networks

The deep learning method opens new doors to designing micro-structured materials effectively by replacing the computationally expensive finite element simulations. Since the neural network (NN) only extrapolates well within

the data domain defined by its database for the training process [11], the coverage of the data domain is important for the applicability of the NN. In material design, the database usually contains pairs of geometry and properties. Its data domain of properties can be represented as a material-property space with properties plotted along each axis [53]. Therefore, the applicability of the NN can be represented by a material-property space containing all property points from the database. In a forward fashion, the maximal space boundary (denoted as a red line in Fig. 26) is treated as a reference to assess the applicability of the NN in predicting material properties. Theoretically, the wider the data domain covers in the maximal material-property space, the better the applicability of its NN is for a specific class of metamaterials defined in the database. Besides, although there has been research about advances in various deeplearning methods for material design problems, database generation has not been thoroughly investigated. A common method of database generation is the uniform sampling of design variables. To compare with our sampling algorithm, a new database of RVE with non-PUCs is built using uniform sampling with the same number of property points, which retrieves a maximal property space. Due to the central limit theorem, most of them (denoted as red dots in Fig. 26) become concentrated around a central position of their distribution and restrict the spread of the data to reach its peripheral unexplored material-property space. In the periphery of the data domain, the lack of data might induce bias and errors during the training process of the NN. On the contrary, during the iterative expansion process, our sampling algorithm continuously generates property points (denoted as blue dots in Fig. 16) to fulfill the region near the space boundary. With the K-function and down-sampling method, our database becomes more evenly distributed and alleviates the issue mentioned above. Moreover, with the same number of samples, our sampling provides wide coverage of the data domain, which provides better applicability for the NN compared to the domain achieved by uniform sampling.

4.3. Uncertainty Quantification in the Property Space

With advances in additive manufacturing resulting in the proliferation of metamaterials, an evaluation of their tolerance to manufacturing defects is vital. Any deviation from the intended geometry is possible to alter the mechanical properties of printed parts. This paper mainly studies the impacts on the structural properties of the CMMs induced by surface distortion during the FFF printing process. In Fig. 24c or 27a, variation intervals of the maximal space boundary allow for visualizing the impacts on combinations of the two properties under consideration, Young's modulus (E_{11}) and Poisson's ratio (v_{12}) . Both Fig. 24c or 27a and Table 4 indicate an approximately linear relationship between variations in the maximal space area and tolerances in geometric variables. In general, as the uncertainty level of design parameters increases, the confidence interval of properties is expanded (Figs. 24a and b), leading to a larger shrinkage of the property space (Fig. 24c or 27a). Besides, the variation interval expands as Young's modulus decreases in Fig. 24c or 27a. It indicates that the defect has less impact on the two properties of RVEs with high E_{11} . The complexity of geometric patterns shown in Fig. 27a appears to explain well the extent of the impact causing the variations in properties. As Young's modulus decreases, the complexities of the pore shapes in RVEs increase, leading to higher uncertainty of mechanical performances. Here, this paper makes a further investigation of an individual property instead of combinations of the two properties. To have a detailed look at the uncertainty, it studies the effect of manufacturing defects on an individual property not only based on property points on the boundary (Fig. 27a) but also on that within the space (Fig. 27b). In Fig. 27b, seven representative property points are selected in the space. Their variation intervals and corresponding geometric patterns indicate a similar trend of uncertainty along with the axis of Young's modulus. Besides, for the selected points in Figs. 27a and b, Table 5 summarizes the average percentage differences (%diff) between their deterministic properties and properties under the three tolerance cases concerning their deterministic properties. The larger percentage values in the first row of Table 5 indicate that Young's modulus of RVEs is more sensitive to surface distortion than Poisson's ratio. The statement is also illustrated by the large shrinkage of the property boundary along the axis of Young's modulus. The above comparison results and statements can also be proven by comparing standard deviations (σ) between the two properties. For these points selected on and within the boundary, the standard deviations of properties are normalized with their extreme values and summarized in Table 6 for the three tolerance cases. From the statistics, the uncertainty in the geometric patterns of the RVEs has a relatively large influence on Young's modulus of the CMMs compared to Poisson's ratio, leading to relatively large percentage differences in Young's modulus.

Table 5: Summary of average percentage differences between deterministic and stochastic properties of the seven selected points under the three tolerance cases

	Case #1 (±10%)	Case #2 (±20%)	Case #3 (±30%)
%diff of E_{11}	0.59%	1.19%	1.79%
%diff of v_{12}	0.56%	1.14%	1.60%

Table 6: Summary of average normalized standard deviations of the seven selected points under the three tolerance cases

	Case #1 (±10%)	Case #2 (±20%)	Case #3 (±30%)
$\sigma_{normalized}$ of E_{11} $\sigma_{normalized}$ of ν_{12}	0.0541	0.1082	0.1623
	0.0488	0.0964	0.1452

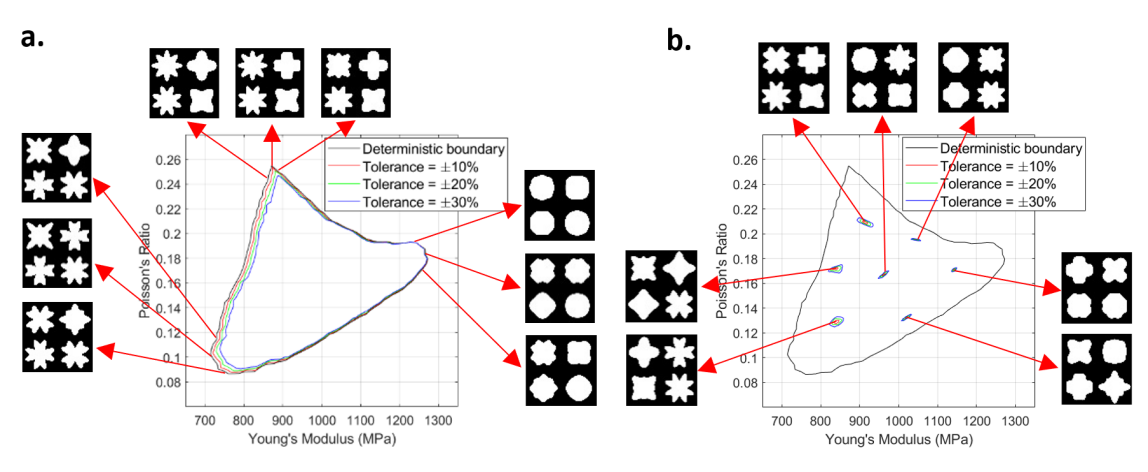


Fig. 27: Variation intervals of the three tolerance cases for property points selected (a) on the maximal material-property space boundary and (b) within the space boundary.

4.4. Future Works

There are some topics worth examination and further study in the future. First, it is not difficult to increase objective properties selected on the space boundary to explore more undiscovered property points that are possibly exterior to the current space. It could lead to a reduction in the number of space expansion loops. However, it is challenging to determine the appropriate amount of possible property points to finalize a material-property space since this requires balancing the benefits of comprehensive solution distributions in the space against the drawbacks of high computational expenses of the GA. The effectiveness of the number and diversity of possible solutions in GA is an essential question for future studies. Secondly, apart from uniform sampling, other random sampling methods are available for sampling objective properties to determine an initial material-property space, such as Latin hypercube sampling, simple sequential inhibition process [54], and nonaligned systematic sampling [55]. These methods produce samples with low discrepancy (dispersed widely within their bounds) while maintaining samples with high diversity (distributed randomly) [55]. It would be interesting to test with new sampling methods and compare areas of their newly generated initial property space.

The paper aims to provide brief insights into uncertainty in combinations of two properties by the visual effect shown as stochastic boundaries of a material-property space. To this end, the surface distortion is simplified as the variation of the geometric parameters. However, a more accurate representation of this defect can be achieved by parameterizing it as the differences of centroid locations, surface curvatures, and areas of the pore between the printed and simulated model. In the future, we plan to physically print our CMMs as thin structural panels and construct this stochastic representation based on the experimental data of our printed models. Similar to the surface distortion,

uncertainty arising from any other manufacturing defects can be efficiently quantified by the Monte Carlo sampling method facilitated by deep learning with fully connected layers as long as the defects can be parameterized [56]. However, in some cases, it may be difficult to parameterize the defects in manufacturing. In such cases, convolutional neural networks (CNNs) can be used to detect manufacturing defects by extracting features from the given images [57, 58, 59]. With the application of CNNs, the stochastic boundaries of material property spaces associated with more complex manufacturing defects can also be determined.

Currently, our study mainly focuses on the linear elastic properties of CMMs under the assumption of small deformations. Accordingly, the displacement of RVEs should be small enough such that the changes in the stiffness of the material due to the loading can be neglected [60]. To determine the nonlinear properties of the CMMs, uniaxial strain tests with a large deformation causing the materials to display plastic or hyper-elastic behavior should be considered [26]. In that case, the effective properties of RVEs are no longer constant like the materials within the elastic region and they vary based on the prescribed boundary condition (specifically uniaxial stains applied on the surface of RVEs) [26]. In the future, our presented material property space framework can be integrated into nonlinear property calculation by utilizing specific boundary conditions.

Lastly, in addition to the two properties studied in this paper, there are many other interesting combinations of properties for various engineering applications, such as porosity and Young's modulus, shear modulus and Young's modulus, etc. The work of Omairey et al. [34] illustrates their proposed ABAQUS plugin called EasyPBC has a wide range of applications for RVEs with isotropic or anisotropic properties, RVEs in 2D or 3D, and RVEs of homogenous or composite materials [34, 61, 62, 63, 64, 65, 66]. In future works, a 2D material property space is developed by EasyPBC to represent mechanical properties along two different directions of their RVEs, such as E_{11} and E_{22} ν_{12} and ν_{21} , etc. It is a possible avenue for further research on many kinds of material-property spaces according to academic and industrial requirements.

5. Conclusion

This paper describes an exploration approach facilitated by the selection algorithm of objective properties and sampling algorithm of property points for mapping a maximal material-property space and generating diverse microstructural sets of cellular metamaterials. The 2D material-property space resulting from the proposed approach is a reliable representation of true combinations of two properties under consideration in academic and industrial applications. Our mapping framework overcomes potential issues of mapping methods in recent studies discussed in the introduction. Unlike the analytical methods (Hashin-Shtrikman, Voigt, and Reuss bounds), our sampling algorithm allows users to explore the space in 2D by solving inverse design problems with multiple objective properties. Compared to the uniform sampling method, our framework progressively expands the incomplete property space to a full closure that provides a relatively more comprehensive estimation of the property space. In addition, the property space boundary is defined by a built-in function in MATLAB called *boundary*. With the benefits of this function, we overcome the issue of GWS and allow the users to define the space boundary that varies from convex to concave surfaces. In comparison with ANSI and AWS which explore the space boundary with gradient-based methods, our mapping framework utilizes a gradient-free method, GA, which is processed with a high mutation rate to prevent fast convergence of optimal solutions while increasing the diversity of the individuals of each generation. This increases the possibility of building an expansive property space.

Besides, the discussion section demonstrates the use of material property spaces of multiple families of the CMM as a material selection chart to effectively screen out the inappropriate families based on their space region and intuitively pick geometric patterns that are easy to manufacture from the overlapping areas. In addition, this paper compares the performance of our proposed sampling algorithm to traditional algorithms for building a database of the NN and finds that our algorithm obtained broader and more evenly distributed property points than traditional algorithms for the same number of samples in the data domain, which guarantees the well-applicability of the NN in the material design problem. As a practical use case, our study considers one of the defects in additive manufacturing, called surface distortion in FFF printing. Uncertainty in the material-property space (combinations of two properties) associated with this defect can be visually demonstrated as variation intervals of its space boundary and numerically represented as variations in its space area under the different tolerance cases.

In this study, this GA-based approach presented a new avenue for exploring a material-property space. It can be extended to map property spaces with other interesting combinations of properties and to investigate more complex

material systems with anisotropic properties in the future.

Data availability

The code used for expanding the material-property space and building the neural network of CMMs has been archived in a GitHub repository (https://github.com/simon941222/Mapping-Material-Property-Space-under-Uncertainty-Isotropic).

Funding

This research was supported by the National Science Foundation (NSF) CMMI Division Grant CMMI-2053840 and NSF CAREER Award CMMI-2236947 (Program Director: Dr. Kathryn Jablokow).

Acknowledgement

The authors would like to acknowledge the assistance provided by Dr. Sadik Omairey in sharing the ABAQUS CAE interface plugin (EasyPBC).

References

- [1] Nieh, T. G. (1997). Processing and modeling of cellular solids for light-weight structures. Office of Scientific and Technical Information (OSTI). https://doi.org/10.2172/611844
- [2] Hu, Z., Thiyagarajan, K., Bhusal, A., Letcher, T., Fan, Q. H., Liu, Q., & Salem, D. (2017). Design of ultra-lightweight and high-strength cellular structural composites inspired by biomimetics. In Composites Part B: Engineering (Vol. 121, pp. 108–121). Elsevier BV. https://doi.org/10.1016/j.compositesb.2017.03.033
- [3] Sairajan, K. K., Aglietti, G. S., & Mani, K. M. (2016). A review of multifunctional structure technology for aerospace applications. In Acta Astronautica (Vol. 120, pp. 30–42). Elsevier BV. https://doi.org/10.1016/j.actaastro.2015.11.024
- [4] Meola, C., Boccardi, S., & Carlomagno, G. maria. (2017). Composite Materials in the Aeronautical Industry. In Infrared Thermography in the Evaluation of Aerospace Composite Materials (pp. 1–24). Elsevier. https://doi.org/10.1016/b978-1-78242-171-9.00001-2
- [5] Su, L., Liu, H., Yao, G., & Zhang, J. (2019). Experimental study on the closed-cell aluminum foam shock absorption layer of a high-speed railway tunnel. In Soil Dynamics and Earthquake Engineering (Vol. 119, pp. 331–345). Elsevier BV. https://doi.org/10.1016/j.soildyn.2019.01.012
- [6] Yao, S., Xiao, X., Xu, P., Qu, Q., & Che, Q. (2018). The impact performance of honeycomb-filled structures under eccentric loading for subway vehicles. In Thin-Walled Structures (Vol. 123, pp. 360–370). Elsevier BV. https://doi.org/10.1016/j.tws.2017.10.031
- [7] Wu, W., Hu, W., Qian, G., Liao, H., Xu, X., & Berto, F. (2019). Mechanical design and multifunctional applications of chiral mechanical metamaterials: A review. In Materials & Samp; Design (Vol. 180, p. 107950). Elsevier BV. https://doi.org/10.1016/j.matdes.2019.107950
- [8] Li, N., Bai, C., & Liu, M. (2022). Configuration-controllable porous metamaterial and its bandgap characteristics: Experimental and numerical analysis. In Journal of Sound and Vibration (Vol. 535, p. 117107). Elsevier BV. https://doi.org/10.1016/j.jsv.2022.117107
- [9] Song, K., Li, D., Liu, T., Zhang, C., Min Xie, Y., & Liao, W. (2022). Crystal-twinning inspired lattice metamaterial for high stiffness, strength, and toughness. In Materials & Samp; Design (Vol. 221, p. 110916). Elsevier BV. https://doi.org/10.1016/j.matdes.2022.110916
- [10] Ashby, M.F., Materials Selection in Mechanical Design, 5 edition, ButterworthHeinemann, Cambridge, MA, 2016.
- [11] Röding, M., Wåhlstrand Skärström, V., & Lorén, N. (2022). Inverse design of anisotropic spinodoid materials with prescribed diffusivity. In Scientific Reports (Vol. 12, Issue 1). Springer Science and Business Media LLC. https://doi.org/10.1038/s41598-022-21451-6
- [12] Hashin, Z., & Shtrikman, S. (1962). A Variational Approach to the Theory of the Effective Magnetic Permeability of Multiphase Materials. In Journal of Applied Physics (Vol. 33, Issue 10, pp. 3125–3131). AIP Publishing. https://doi.org/10.1063/1.1728579
- [13] Voigt, W., Lehrbuch der Kristallphysik, B.G. Teubner Verlag, Leipzig, 1928.
- [14] Reuss, A. (1929) Berechnung der Fliessgrenze von Mischkristallen auf Grund der Plastizitätsbedingung für Einkristalle. ZAMM—Journal of Applied Mathematics and Mechanics/Zeitschrift für Angewandte Mathematik und Mechanik, 9, 49-58. http://dx.doi.org/10.1002/zamm.19290090104
- [15] Adams, B.L., Kalidindi, S.R., Fullwood, D.T., Microstructure-sensitive Design for Performance Optimization, 1 edition, Butterworth-Heinemann, 2012.
- [16] Fast, T., Knezevic, M., & Kalidindi, S. R. (2008). Application of microstructure sensitive design to structural components produced from hexagonal polycrystalline metals. In Computational Materials Science (Vol. 43, Issue 2, pp. 374–383). Elsevier BV. https://doi.org/10.1016/j.commatsci.2007.12.002
- [17] Proust, G., & Kalidindi, S. (2006). Procedures for construction of anisotropic elastic-plastic property closures for face-centered cubic polycrystals using first-order bounding relations. In Journal of the Mechanics and Physics of Solids (Vol. 54, Issue 8, pp. 1744–1762). Elsevier BV. https://doi.org/10.1016/j.jmps.2006.01.010
- [18] Kim, T., Elango, P., Malyuta, D., & Acikmese, B. (2022). Guided Policy Search using Sequential Convex Programming for Initialization of Trajectory Optimization Algorithms. In 2022 American Control Conference (ACC). 2022 American Control Conference (ACC). IEEE. https://doi.org/10.23919/acc53348.2022.9867151

- [19] Li, J., Guo, H., Sun, P., Wang, Y., Huang, S., Yuan, T., & Zhang, H. (2022). Topology optimization of anisotropy hierarchical honeycomb acoustic metamaterials for extreme multi-broad band gaps. In Mechanics of Advanced Materials and Structures (pp. 1–13). Informa UK Limited. https://doi.org/10.1080/15376494.2022.2079027
- [20] Meng, H., Chronopoulos, D., Fabro, A. T., Maskery, I.,& Chen, Y. (2020). Optimal design of rainbow elastic metamaterials. In International Journal of Mechanical Sciences (Vol. 165, p. 105185). Elsevier BV. https://doi.org/10.1016/j.ijmecsci.2019.105185
- [21] Jian, Y., Tang, L., Hu, G., Wang, Y., & Aw, K. C. (2022). Adaptive genetic algorithm enabled tailoring of piezoelectric metamaterials for optimal vibration attenuation. In Smart Materials and Structures (Vol. 31, Issue 7, p. 075026). IOP Publishing. https://doi.org/10.1088/1361-665x/ac775d
- [22] Dos Reis, F., & Karathanasopoulos, N. (2022). Inverse metamaterial design combining genetic algorithms with asymptotic homogenization schemes. In International Journal of Solids and Structures (Vol. 250, p. 111702). Elsevier BV. https://doi.org/10.1016/j.ijsolstr.2022.111702
- [23] Luo, P., Lan, G., Nong, J., Zhang, X., Xu, T., & Wei, W. (2022). Broadband coherent perfect absorption employing an inverse-designed meta-surface via genetic algorithm. In Optics Express (Vol. 30, Issue 19, p. 34429). Optica Publishing Group. https://doi.org/10.1364/oe.468842
- [24] Liu, S., & Acar, P. (2022). Inverse Multiscale Design of Cellular Mechanical Metamaterials. In AIAA SCITECH 2022 Forum. AIAA SCITECH 2022 Forum. American Institute of Aeronautics and Astronautics. https://doi.org/10.2514/6.2022-1135
- [25] Sumida, B. H., Houston, A. I., McNamara, J. M., & Hamilton, W. D. (1990). Genetic algorithms and evolution. In Journal of Theoretical Biology (Vol. 147, Issue 1, pp. 59–84). Elsevier BV. https://doi.org/10.1016/s0022-5193(05)80252-8
- [26] Xue, T., Beatson, A., Chiaramonte, M., Roeder, G., Ash, J. T., Menguc, Y., Adriaenssens, S., Adams, R. P., & Mao, S. (2020). A data-driven computational scheme for the nonlinear mechanical properties of cellular mechanical metamaterials under large deformation. In Soft Matter (Vol. 16, Issue 32, pp. 7524–7534). Royal Society of Chemistry (RSC). https://doi.org/10.1039/d0sm00488j
- [27] Kumar, A., Datta, S., Roy, T., & Mahapatra, S. S. (2022). Parametric studies of fused filament fabrication towards fabrication of 2D auxetic metamaterial cellular structure followed by auxeticity simulation. In Sādhanā (Vol. 47, Issue 4). Springer Science and Business Media LLC. https://doi.org/10.1007/s12046-022-01993-1
- [28] Yadav, A., Rohru, P., Babbar, A., Kumar, R., Ranjan, N., Chohan, J. S., Kumar, R., & Gupta, M. (2022). Fused filament fabrication: A state-of-the-art review of the technology, materials, properties and defects. In International Journal on Interactive Design and Manufacturing (IJIDeM). Springer Science and Business Media LLC. https://doi.org/10.1007/s12008-022-01026-5
- [29] López, F. (2020). TPOT: Pipelines optimization with genetic algorithms. Medium. Retrieved August 30, 2022, from https://towardsdatascience.com/tpot-pipelines-optimization-with-genetic-algorithms-56ec44ef6ede
- [30] Yu, X., Zhou, J., Liang, H., Jiang, Z., & Wu, L. (2018). Mechanical metamaterials associated with stiffness, rigidity and compressibility: A brief review. In Progress in Materials Science (Vol. 94, pp. 114–173). Elsevier BV. https://doi.org/10.1016/j.pmatsci.2017.12.003
- [31] Kelkar, P. U., Kim, H. S., Cho, K.-H., Kwak, J. Y., Kang, C.-Y., & Song, H.-C. (2020). Cellular Auxetic Structures for Mechanical Metamaterials: A Review. In Sensors (Vol. 20, Issue 11, p. 3132). MDPI AG. https://doi.org/10.3390/s20113132
- [32] Zadpoor, A. A. (2016). Mechanical meta-materials. In Materials Horizons (Vol. 3, Issue 5, pp. 371–381). Royal Society of Chemistry (RSC). https://doi.org/10.1039/c6mh00065g
- [33] Surjadi, J. U., Gao, L., Du, H., Li, X., Xiong, X., Fang, N. X., & Lu, Y. (2019). Mechanical Metamaterials and Their Engineering Applications. In Advanced Engineering Materials (Vol. 21, Issue 3, p. 1800864). Wiley. https://doi.org/10.1002/adem.201800864
- [34] Omairey, S. L., Dunning, P. D., & Sriramula, S. (2018). Development of an ABAQUS plugin tool for periodic RVE homogenisation. In Engineering with Computers (Vol. 35, Issue 2, pp. 567–577). Springer Science and Business Media LLC. https://doi.org/10.1007/s00366-018-0616-4
- [35] Tung, L. V., Ha-Van, N., & Seo, C. (2020). A Novel Metamaterial Design Using Genetic Algorithm for High Gain Energy Harvesting Antenna. In 2020 IEEE Wireless Power Transfer Conference (WPTC). 2020 IEEE Wireless Power Transfer Conference (WPTC). IEEE. https://doi.org/10.1109/wptc48563.2020.9295587
- [36] Chen, P. Y., Chen, C. H., Wang, H., Tsai, J. H., & Ni, W. X. (2008). Synthesis design of artificial magnetic metamaterials using a genetic algorithm. In Optics Express (Vol. 16, Issue 17, p. 12806). Optica Publishing Group. https://doi.org/10.1364/oe.16.012806
- [37] "Boundary of a set of points in 2-D or 3-D." MATLAB. https://www.mathworks.com/help/matlab/ref/boundary.html. Accessed May 30, 2023.
- [38] Črepinšek, M., Liu, S.-H., & Mernik, M. (2013). Exploration and exploitation in evolutionary algorithms. In ACM Computing Surveys (Vol. 45, Issue 3, pp. 1–33). Association for Computing Machinery (ACM). https://doi.org/10.1145/2480741.2480752
- [39] Srinivas, M., & Patnaik, L. M. (1994). Genetic algorithms: a survey. In Computer (Vol. 27, Issue 6, pp. 17–26). Institute of Electrical and Electronics Engineers (IEEE). https://doi.org/10.1109/2.294849
- [40] Shahbazi, Z., & Byun, Y.-C. (2022). An Optimized Ensemble Model for Prediction the Bandwidth of Metamaterial Antenna. In Computers, Materials & Continua (Vol. 71, Issue 1, pp. 199–213). Computers, Materials and Continua (Tech Science Press). https://doi.org/10.32604/cmc.2022.021886
- [41] SABIC Innovative Plastics ULTEM 1000R PEI, http://www.lookpolymers.com/polymer_SABIC-Innovative-Plastics-ULTEM-1000R -PEI.php. Accessed March 18, 2020.
- [42] Liu, S., & Acar, P. (2023). Parameter Space Exploration of Cellular Mechanical Metamaterials Using Genetic Algorithms. In AIAA Journal (pp. 1–11). American Institute of Aeronautics and Astronautics (AIAA). https://doi.org/10.2514/1.j062864
- [43] Wickramasinghe, S., Do, T., & Tran, P. (2020). FDM-Based 3D Printing of Polymer and Associated Composite: A Review on Mechanical Properties, Defects and Treatments. In Polymers (Vol. 12, Issue 7, p. 1529). MDPI AG. https://doi.org/10.3390/polym12071529
- [44] Butt, J., & Bhaskar, R. (2020). Investigating the Effects of Annealing on the Mechanical Properties of FFF-Printed Thermoplastics. In Journal of Manufacturing and Materials Processing (Vol. 4, Issue 2, p. 38). MDPI AG. https://doi.org/10.3390/jmmp4020038
- [45] Sunny, S., Chen, H., Malik, A., & Lu, H. (2021). Influence of residual stress and fluid–structure interaction on the impact behavior of fused filament fabrication components. In Additive Manufacturing (Vol. 37, p. 101662). Elsevier BV. https://doi.org/10.1016/j.addma.2020.101662
- [46] "Accuracies and Tolerances in 3D Printing." 3Faktur, November 12, 2019. https://3faktur.com/en/accuracies-and-tolerances-in-3d-printing/. Accessed June 3, 2023.
- [47] Minetola, P., Calignano, F., & Galati, M. (2020). Comparing geometric tolerance capabilities of additive manufacturing systems for polymers. In Additive Manufacturing (Vol. 32, p. 101103). Elsevier BV. https://doi.org/10.1016/j.addma.2020.101103

- [48] Haase, P. (1995). Spatial pattern analysis in ecology based on Ripley's K-function: Introduction and methods of edge correction. In Journal of Vegetation Science (Vol. 6, Issue 4, pp. 575–582). Wiley. https://doi.org/10.2307/3236356
- [49] Zimmerman, R. W. (1992). Hashin-Shtrikman bounds on the Poisson ratio of a composite material. In Mechanics Research Communications (Vol. 19, Issue 6, pp. 563–569). Elsevier BV. https://doi.org/10.1016/0093-6413(92)90085-0
- [50] Jahan, A., Edwards, K. L., & Dahraminasab, M. (2016). Multi-criteria decision analysis: For supporting the selection of engineering materials in product design. Butterworth-Heinemann.
- [51] Shercliff, H. R., & Ashby, M. F. (2016). Elastic Structures in Design. In Reference Module in Materials Science and Materials Engineering. Elsevier. https://doi.org/10.1016/b978-0-12-803581-8.02944-1
- [52] Alghamdy, M., Ahmad, R., & Alsayyed, B. (2019). Material Selection Methodology for Additive Manufacturing Applications. In Procedia CIRP (Vol. 84, pp. 486–490). Elsevier BV. https://doi.org/10.1016/j.procir.2019.04.265
- [53] Zheng, X., Chen, T.-T., Guo, X., Samitsu, S., & Watanabe, I. (2021). Controllable inverse design of auxetic metamaterials using deep learning. In Materials & Design (Vol. 211, p. 110178). Elsevier BV. https://doi.org/10.1016/j.matdes.2021.110178
- [54] Dekkers, A., & Aarts, E. (1991). Global optimization and simulated annealing. In Mathematical Programming (Vol. 50, Issues 1–3, pp. 367–393). Springer Science and Business Media LLC. https://doi.org/10.1007/bf01594945
- [55] Maaranen, H., Miettinen, K. & Penttinen, A. On initial populations of a genetic algorithm for continuous optimization problems. J Glob Optim 37, 405–436 (2007). https://doi.org/10.1007/s10898-006-9056-6
- [56] Yang, J., Li, S., Wang, Z., Dong, H., Wang, J., & Tang, S. (2020). Using Deep Learning to Detect Defects in Manufacturing: A Comprehensive Survey and Current Challenges. In Materials (Vol. 13, Issue 24, p. 5755). MDPI AG. https://doi.org/10.3390/ma13245755
- [57] Perez, H., Tah, J. H. M., & Mosavi, A. (2019). Deep Learning for Detecting Building Defects Using Convolutional Neural Networks. In Sensors (Vol. 19, Issue 16, p. 3556). MDPI AG. https://doi.org/10.3390/s19163556
- [58] Dimitriou, N., Leontaris, L., Vafeiadis, T., Ioannidis, D., Wotherspoon, T., Tinker, G., & Tzovaras, D. (2020). A Deep Learning framework for simulation and defect prediction applied in microelectronics. In Simulation Modelling Practice and Theory (Vol. 100, p. 102063). Elsevier BV. https://doi.org/10.1016/j.simpat.2019.102063
- [59] Yang, J., Li, S., Wang, Z., & Yang, G. (2019). Real-Time Tiny Part Defect Detection System in Manufacturing Using Deep Learning. In IEEE Access (Vol. 7, pp. 89278–89291). Institute of Electrical and Electronics Engineers (IEEE). https://doi.org/10.1109/access.2019.2925561
- [60] Wenz, F., Schmidt, I., Leichner, A., Lichti, T., Baumann, S., Andrae, H., & Eberl, C. (2021). Designing Shape Morphing Behavior through Local Programming of Mechanical Metamaterials. In Advanced Materials (Vol. 33, Issue 37). Wiley. https://doi.org/10.1002/adma.202008617
- [61] Fong, E., Omairey, S. L., & Dunning, P. D. (2020). Design of multifunctional metamaterials using optimization (Version 1). arXiv. https://doi.org/10.48550/ARXIV.2004.13571
- [62] Orlova, D. A., Panchenko, A. Yu., Omairey, S. L., & Berinskii, I. E. (2022). Computational homogenization of bio-inspired metamaterial with a random fiber network microstructure. In Mechanics Research Communications (Vol. 124, p. 103930). Elsevier BV. https://doi.org/10.1016/j.mechrescom.2022.103930
- [63] Sangsefidi, A. R., Dibajian, S. H., Kadkhodapour, J., Anaraki, A. P., Schmauder, S., & Schneider, Y. (2021). An Abaqus plugin for evaluation of the Auxetic structure performance. In Engineering with Computers (Vol. 38, Issue S2, pp. 1681–1704). Springer Science and Business Media LLC. https://doi.org/10.1007/s00366-021-01295-w
- [64] Zhao, Y., Wang, Y., Hao, J., Wang, Y., Wang, K., & Tai, S. (2023). Study on mechanical properties of cellular structures with negative Poisson's ratio based on the development of Abaqus plug-in tool. In Composite Structures (Vol. 322, p. 117348). Elsevier BV. https://doi.org/10.1016/j.compstruct.2023.117348
- [65] Schwahofer, O., Büttner, S., Binder, J., Colin, D., & Drechsler, K. (2022). Multiscale Optimization of 3D-Printed Beam-Based Lattice Structures through Elastically Tailored Unit Cells. In Advanced Engineering Materials (Vol. 25, Issue 20). Wiley. https://doi.org/10.1002/adem.202201385
- [66] Zhu, L., Wang, X., Sun, L., Hu, Q., & Li, N. (2022). Optimisation of Selective Laser Melted Ti6Al4V Functionally Graded Lattice Structures Accounting for Structural Safety. In Materials (Vol. 15, Issue 24, p. 9072). MDPI AG. https://doi.org/10.3390/ma15249072